PTBP1 promotes hematopoietic stem cell maintenance and red blood cell development by ensuring sufficient availability of ribosomal constituents

Rehn, Matilda; Wenzel, Anne; Frank, Anne-Katrine; Schuster, Mikkel Bruhn; Pundhir, Sachin; Jørgensen, Nanna; Vitting-Seerup, Kristoffer; Ge, Ying; Jendholm, Johan; Michaut, Magali

Total number of authors:
20

Published in:
Cell Reports

Link to article, DOI:
10.1016/j.celrep.2022.110793

Publication date:
2022

Document Version
Publisher's PDF, also known as Version of record

Cell Reports

Article

PTBP1 promotes hematopoietic stem cell maintenance and red blood cell development by ensuring sufficient availability of ribosomal constituents

Graphical abstract

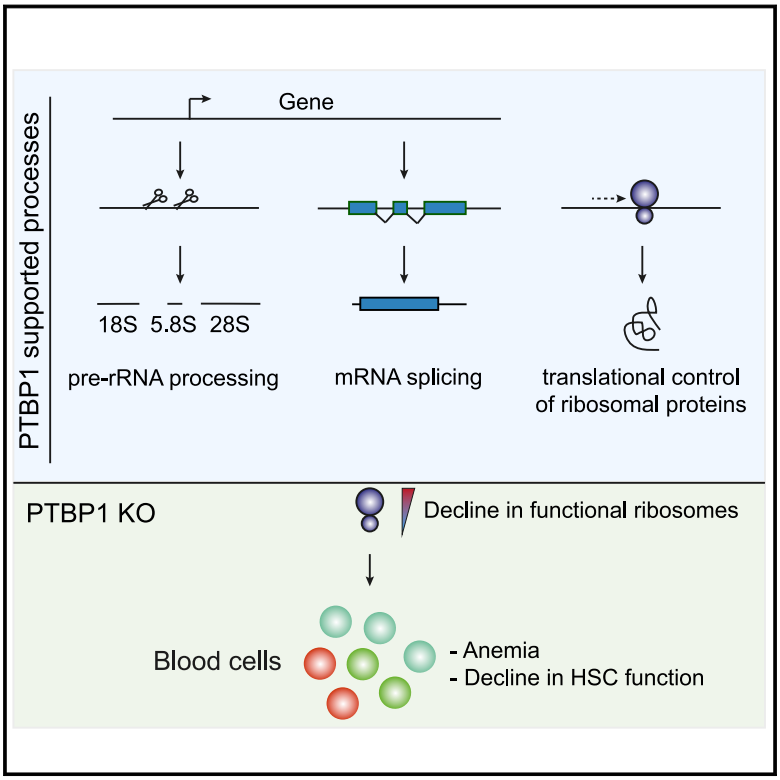

Authors

Matilda Rehn, Anne Wenzel, Anne-Katrine Frank, ..., Martin Holzenberger, Dimitri G. Pestov, Bo Torben Porse

Correspondence

bo.porse@finsenlab.dk

In brief

Congenital ribosomopathies are caused by mutations in genes affecting ribosome biogenesis or function. Rehn et al. find that loss of the splicing regulator, PTBP1, within murine hematopoiesis is associated with reduced protein synthesis, anemia, and reduced stem cell function, thereby mirroring ribosomopathy. These findings identify PTBP1 as a ribosome-integrating factor.

Highlights

- Loss of PTBP1 leads to anemia and a decline in hematopoietic stem cell function
- Loss of PTBP1 leads to a reduction in protein synthesis in hematopoietic cells
- PTBP1 is required for the generation of key ribosomal constituents
- PTPB1 constitutes an integrator of ribosome function

Rehn et al., 2022, Cell Reports *39*, 110793
May 10, 2022
https://doi.org/10.1016/j.celrep.2022.110793

CellPress

Cell Reports

CellPress
OPEN ACCESS

Article

PTBP1 promotes hematopoietic stem cell maintenance and red blood cell development by ensuring sufficient availability of ribosomal constituents

Matilda Rehn,[1,2,3] Anne Wenzel,[1,2,3] Anne-Katrine Frank,[1,2,3] Mikkel Bruhn Schuster,[1,2,3] Sachin Pundhir,[1,2,3] Nanna Jørgensen,[1,2,3] Kristoffer Vitting-Seerup,[2] Ying Ge,[1,2,3] Johan Jendholm,[1,2,3] Magali Michaut,[1,2,3] Erwin M. Schoof,[1,2,3,4] Tanja Lyholm Jensen,[1,2,3] Nicolas Rapin,[1,2,3] Russell T. Sapio,[5] Kasper Langebjerg Andersen,[2] Anders H. Lund,[2] Michele Solimena,[6,7,8,9] Martin Holzenberger,[10] Dimitri G. Pestov,[5] and Bo Torben Porse[1,2,3,11,*]

[1]The Finsen Laboratory, Rigshospitalet, Faculty of Health Sciences, University of Copenhagen, 2200 Copenhagen, Denmark
[2]Biotech Research and Innovation Center (BRIC), University of Copenhagen, 2200 Copenhagen, Denmark
[3]Novo Nordisk Foundation Center for Stem Cell Biology, DanStem, Faculty of Health Sciences, University of Copenhagen, 2200 Copenhagen, Denmark
[4]DTU Bioengineering, Danish Technical University, 2800 Kgs. Lyngby, Denmark
[5]Department of Cell Biology and Neuroscience, Rowan University School of Osteopathic Medicine, Stratford, NJ 08084, USA
[6]Molecular Diabetology, University Hospital and Faculty of Medicine, Technische Universität Dresden, Dresden, Germany
[7]Paul Langerhans Institute Dresden of the Helmholtz Center Munich at University Hospital and Faculty of Medicine, Technische Universität Dresden, Dresden, Germany
[8]Max Planck Institute for Molecular Cell Biology and Genetics, Dresden, Germany
[9]German Center for Diabetes Research (DZD e.V.), Neuherberg, Germany
[10]Sorbonne University, INSERM, Research Center Saint-Antoine, CRSA, 75012 Paris, France
[11]Lead contact
*Correspondence: bo.porse@finsenlab.dk
https://doi.org/10.1016/j.celrep.2022.110793

SUMMARY

Ribosomopathies constitute a range of disorders associated with defective protein synthesis mainly affecting hematopoietic stem cells (HSCs) and erythroid development. Here, we demonstrate that deletion of poly-pyrimidine-tract-binding protein 1 (PTBP1) in the hematopoietic compartment leads to the development of a ribosomopathy-like condition. Specifically, loss of PTBP1 is associated with decreases in HSC self-renewal, erythroid differentiation, and protein synthesis. Consistent with its function as a splicing regulator, PTBP1 deficiency results in splicing defects in hundreds of genes, and we demonstrate that the up-regulation of a specific isoform of CDC42 partly mimics the protein-synthesis defect associated with loss of PTBP1. Furthermore, PTBP1 deficiency is associated with a marked defect in ribosome biogenesis and a selective reduction in the translation of mRNAs encoding ribosomal proteins. Collectively, this work identifies PTBP1 as a key integrator of ribosomal functions and highlights the broad functional repertoire of RNA-binding proteins.

INTRODUCTION

Hematopoiesis is the process by which large numbers of mature blood cells are produced through the coordination of self-renewal and lineage commitment undertaken by hematopoietic stem cells (HSCs), followed by expansion and differentiation toward the functional cells of the blood system. The many fate options faced by hematopoietic cells are controlled by integration of internal and external cues, ultimately affecting gene expression (Orkin and Zon, 2008). Although a lot of the associated decisive events occur at the level of transcriptional initiation, increasing evidence suggests that posttranscriptional processes play a fundamental role in shaping gene expression and therefore constitute an important level of gene regulation with the potential to affect cell-fate decisions in both healthy and diseased tissues (Brinegar and Cooper, 2016). Among the main players in posttranscriptional control are RNA-binding proteins (RBPs), which control multiple aspects of RNA processing such as pre-mRNA splicing, cleavage and polyadenylation, RNA stability, localization, editing, and translation. Recent estimations identify more than 1,500 RBPs in humans, of which a large proportion has not been annotated functionally (Gerstberger et al., 2014; Hentze et al., 2018). Some RBPs are now emerging as regulators capable of acting on several RNA-processing steps or RNA types simultaneously (Corsini et al., 2018; Licatalosi et al., 2008).

Pre-mRNA splicing is a process with the potential to generate multiple mRNA isoforms from a single gene, thereby contributing to proteome diversity and gene regulation. As such, alternative mRNA splicing governs many developmental differentiation processes, where stage-specific splicing networks affect

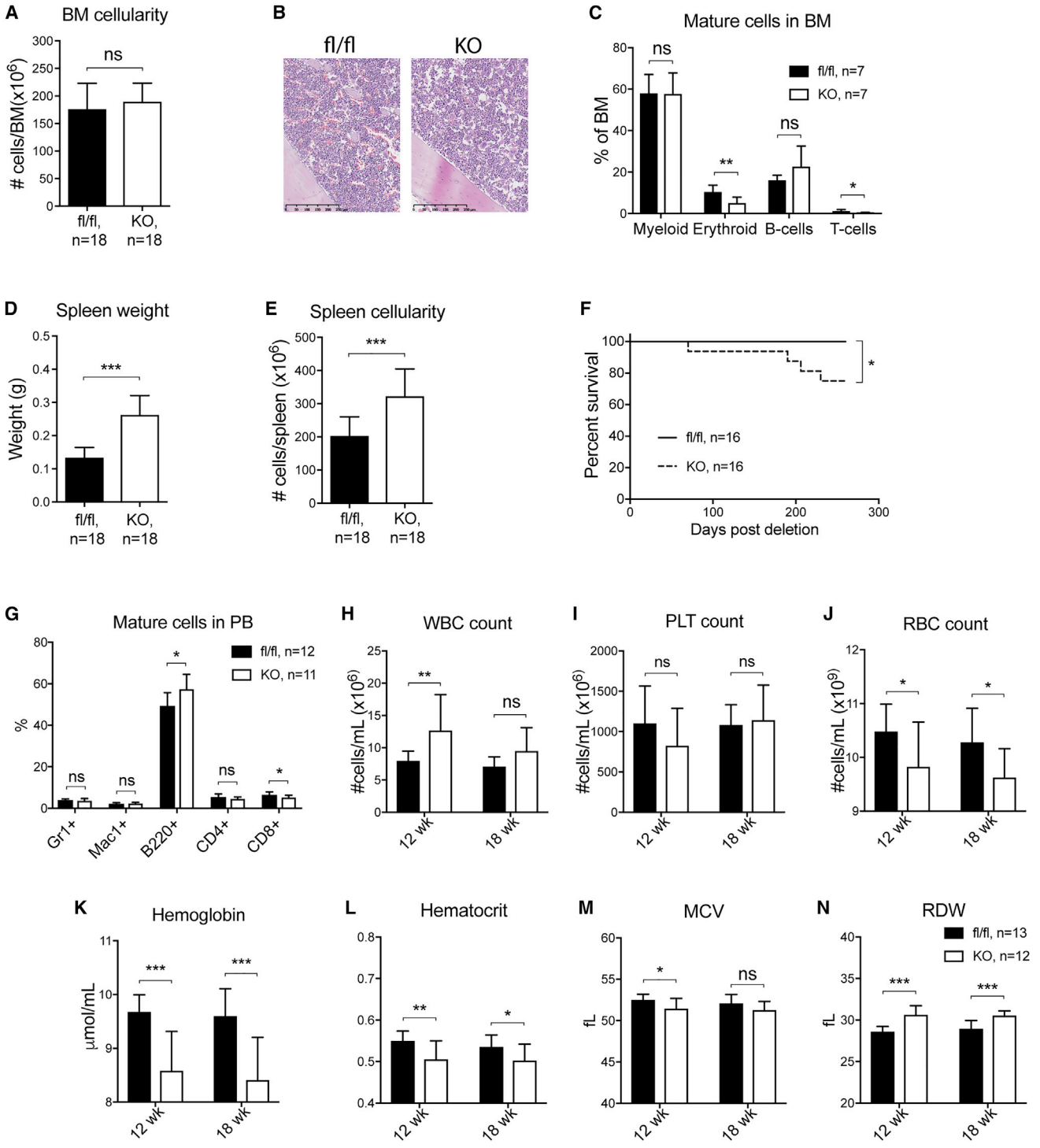

Figure 1. *Ptbp1* deficiency leads to altered hematopoiesis

(A) BM mononuclear cell counts per two hindlimbs.

(B) Hematoxylin and eosin staining of femur sections. Images were scanned by NanoZoomer-XR digital slide scanner and captured by NDP.view 2 at 10× resolution. Scale bar, 250 μm.

(C) Frequencies of $Mac1^+/Gr1^+$, $Ter119^+$, $B220^+$, and $CD4^+/CD8^+$ cells in BM.

(D) Spleen weight.

(E) Spleen cellularity.

(F) Survival post *Ptbp1* deletion.

(legend continued on next page)

self-renewal and differentiation in both normal and malignant tissues. Developmental pre-mRNA splicing networks have been particularly well-characterized in neuronal, muscular, and heart development where several key RBPs with splicing modulatory functions have been identified (Baralle and Giudice, 2017). One of the best-described splicing factors in developmental biology is poly-pyrimidine-tract-binding protein 1 (PTBP1), which belongs to the heterogeneous nuclear ribonucleoprotein (hnRNP) family. PTBP1 is instrumental in early lineage commitment of neuronal precursors by controlling the splicing-dependent degradation of functional *PTBP2* transcripts and by affecting splicing of multiple neuronal pre-mRNAs (Boutz et al., 2007). The power of PTBP1-directed alternative splicing (AS) in neurogenesis is underlined further by studies showing that PTBP1 down-regulation reprograms fibroblasts toward a neuronal fate (Xue et al., 2013). Overexpression of PTBP1 has been associated with several cancer types and induction of oncogenic splice variants affecting metabolism, invasion, and survival (Bielli et al., 2018; He et al., 2014). In addition to its function in AS, PTBP1 has also been shown to be involved in other mRNA processes including 3′-end processing and internal ribosome entry site (IRES)-mediated protein translation (Mitchell et al., 2005; Sawicka et al., 2008). Finally, several studies have linked PTBP1 to functions of long non-coding RNAs (Liu et al., 2018; Sun et al., 2018; Yap et al., 2018).

Ribosomal biogenesis requires a large diversity of RBPs that orchestrate pre-rRNA transcript processing, rRNA base modifications, folding, and transport, ultimately leading to the formation of mature ribosomes. Although all cells rely on efficient protein synthesis, the maintenance and differentiation of embryonic and adult stem cells are particularly dependent on the tight control of this process (Blanco et al., 2016; Corsini et al., 2018; Signer et al., 2014; Tahmasebi et al., 2018). In hematopoiesis, HSCs and erythrocytes are especially sensitive to perturbations in ribosomal function (Signer et al., 2014). This is illustrated further by a group of congenital bone marrow (BM) disorders termed ribosomopathies, characterized by mutations in genes encoding ribosome biogenesis factors or ribosomal proteins (Mills and Green, 2017). The translational output of mRNAs encoding components of the protein-synthesis apparatus is typically dependent on *cis*-regulatory elements in their 5′ UTRs (5′ TOP [terminal oligopyrimidine] motifs) through which the translational rates can be coordinately controlled. It is likely that this type of regulation is necessary to ensure that the highly energy-consuming process of protein translation can be adjusted to meet changes in the environment. Following the early demonstration of TOP motifs and their importance for the translational regulation of ribosomal proteins (Jefferies et al., 1994), the exact identity of such pyrimidine motifs has been challenged (Eliseeva et al., 2013; Hsieh et al., 2012; Thoreen et al., 2012). Thus, it now seems that the *cis*-acting elements of transcripts with coordinated translational regulation can be more widely defined, both in terms of their position in the 5′ UTR (Hsieh et al., 2012) and their composition and lengths (Eliseeva et al., 2013; Hsieh et al., 2012; Thoreen et al., 2012).

Our recognition of the functional importance of RBPs in the context of hematopoiesis stems from studies of factors with links to ribosomopathies and a group of splicing factors, such as SRSF2 and U2AF1, which are frequently mutated in myelodysplastic syndrome (MDS) and acute myeloid leukemia (AML) (Inoue et al., 2016). By contrast, little information exists for PTBP1, which has only been reported to play a role in the function of marginal zone B cells (Monzon-Casanova et al., 2018).

Given the important function of PTBP1 in directing lineage choice in diverse stem cell systems and the overall relevance of mRNA splicing in hematopoiesis, we hypothesized that PTBP1 might play a role as a regulator of posttranscriptional decision events in a hematopoietic context. Indeed, we find that mice lacking PTBP1 in hematopoietic cells develop a ribosomopathy-like condition characterized by inefficient erythropoiesis, anemia and reduced HSC function. Accordingly, our data demonstrate reduced protein synthesis in PTBP1-deficient cells. Mechanistic analyses revealed a function for PTBP1 as a key integrator of ribosome biogenesis and function.

RESULTS

PTBP1 deficiency alters hematopoiesis and results in anemia

To investigate the potential role of PTBP1 in hematopoiesis, we characterized lineage distributions in the BM and blood of *Ptbp1*$^{fl/fl}$; *Mx1Cre* mice in which *Ptbp1* was deleted via poly-IC injections 3 weeks earlier (Figure S1A). Overall BM cellularity and anatomy were unchanged (Figures 1A and 1B). The distribution of myeloid cells (Mac1$^+$/Gr1$^+$) and B cells (B220$^+$) in the BM was normal, while we noted a decrease in erythroid cells (Ter119$^+$) and T cells (CD4$^+$/CD8$^+$) in *Ptbp1*-deficient BM (called *Ptbp1*$^{\Delta/\Delta}$; *Ptbp1*^{KO} from now on) compared with *Ptbp1*$^{fl/fl}$ controls (Figure 1C). Spleen cellularity and weight were pronouncedly increased in *Ptbp1*^{KO} mice, indicative of extramedullary hematopoiesis (Figures 1D and 1E). Furthermore, long-term survival was reduced in the *Ptbp1*^{KO} group (Figure 1F). Analysis of peripheral blood (PB) 8 weeks postdeletion demonstrated a slight skewing within the lymphoid compartment (Figure 1G). The total numbers of white blood cells were transiently increased in PB while platelet counts were normal (Figures 1H and 1I).

(G) Lineage distribution in PB 8 weeks post poly-IC.
(H) PB white blood cell (WBC) count 12 and 18 weeks post poly-IC.
(I) PB platelet (PLT) count 12 and 18 weeks post poly-IC.
(J) PB RBC count 12 and 18 weeks post poly-IC.
(K) Hemoglobin levels in PB 12 and 18 weeks post poly-IC.
(L) Hematocrit in PB 12 and 18 weeks post poly-IC.
(M) Mean cell volume (MCV) in PB 12 and 18 weeks post poly-IC.
(N) Red cell distribution width (RDW) in PB 12 and 18 weeks post poly-IC.
Error bars indicate SD. Statistical analyses were performed using unpaired, two-tailed Student's t test.
See also Figure S1.

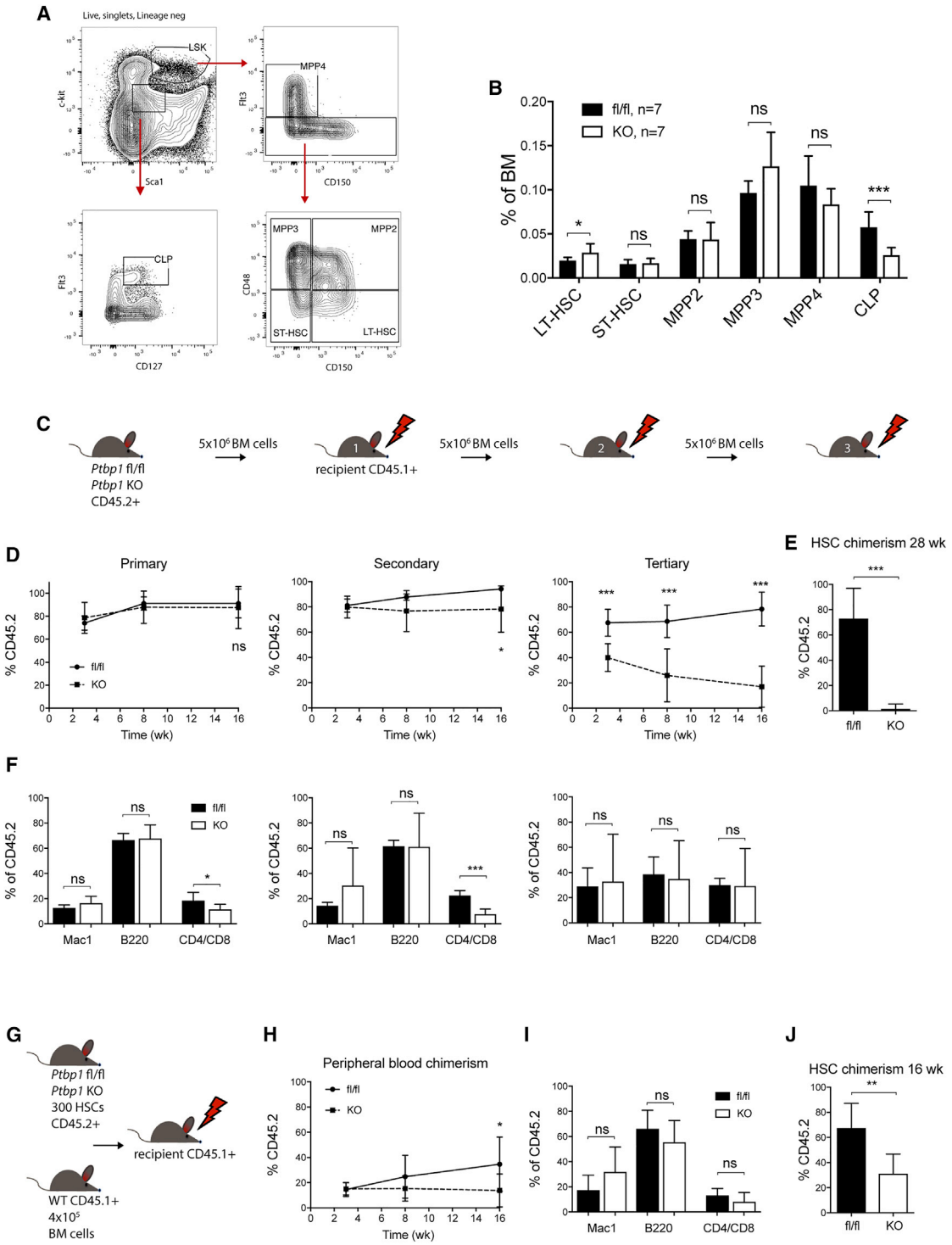

Figure 2. Loss of *Ptbp1* leads to increased numbers of LT-HSCs that are functionally impaired

(A) Flow-cytometry gating used to discern HSPC populations in BM (Pietras et al., 2015).

(B) Quantification of HSPCs in BM from (A).

(C) Overview of the non-competitive serial BM transplantation experiments.

(D) PB donor reconstitution in primary, secondary, and tertiary recipients.

(E) Donor-cell chimerism within the LSK CD150^{+} CD48^{-} compartment in tertiary recipients 28 weeks posttransplantation.

(F) PB lineage distribution within the donor-cell compartment in primary, secondary, and tertiary recipients.

(legend continued on next page)

However, red blood cell (RBC) numbers, hematocrit, hemoglobin levels, RBC size, and RBC size distribution were slightly, but significantly, changed in PB of *Ptbp1*^{KO} mice, demonstrating that loss of PTBP1 promotes anemia (Figures 1J–1N).

In all, loss of PTBP1 leads to a slightly skewed distribution of mature cells in BM and PB, extramedullary hematopoiesis, and decreased long-term survival, as well as development of anemia.

Loss of PTBP1 leads to increased frequencies of LT-HSCs that are functionally impaired

To investigate how loss of PTBP1 affects the numbers of hematopoietic stem and progenitor cells (HSPCs), we performed fluorescence-activated cell sorting (FACS) analysis of BM cells from *Ptbp1*^{KO} and *Ptbp1*$^{fl/fl}$ mice (Pietras et al., 2015). We found a slight increase in the frequency of long-term HSCs (LT-HSCs), while short-term HSCs (ST-HSCs) and multipotent progenitors (MPPs) were unaffected. At the same time, a clear decrease in the frequency of common lymphoid progenitors (CLPs) was detected in *Ptbp1*^{KO} BM (Figures 2A and 2B). To investigate if loss of PTBP1 affects HSC function, we performed both non-competitive and competitive transplantation assays and found that unfractionated BM cells from *Ptbp1*^{KO} or *Ptbp1*$^{fl/fl}$ mice displayed similar contribution to PB, irrespective of the transplantation modality (Figures 2C, 2D, and S1B–S1D). However, serial-transplantation experiments showed that HSC engraftment capacity gradually declined in secondary and tertiary recipients of *Ptbp1*^{KO} cells and that their contribution to the HSC compartment in tertiary recipients was essentially lost (Figures 2C–2E, and S1E–S1G). Consistent with the untransplanted setting, *Ptbp1*^{KO} cells displayed a decrease in T cell output in primary and secondary recipients, which appeared to be lost in tertiary recipients, likely due to low numbers of donor cells, hampering precise assessment of donor lineage distribution (Figure 2F).

To further consolidate the impact of *Ptbp1* deletion on HSC function, we next performed a competitive repopulation assay using FACS-sorted *Ptbp1*^{KO} and *Ptbp1*$^{fl/fl}$ HSCs (Lin$^-$, Sca-1$^+$, c-kit$^+$ [LSK], CD150$^+$, CD48$^-$). This revealed a marked reduction in the contribution of *Ptbp1*^{KO} HSCs to PB chimerism, as well as to the HSC pool at the experimental endpoint (Figures 2G–2J). Finally, we wanted to exclude the possibility that *Mx1Cre*-driven deletion of *Ptbp1* in BM mesenchymal cell populations affected hematopoietic properties (Park et al., 2012). To do so, we performed a reverse-transplantation experiment where *Ptbp1*^{KO} and *Ptbp1*$^{fl/fl}$ mice were used as recipients for wild-type BM cells. Exposure to a *Ptbp1*^{KO} environment for 16 weeks did not influence HSC function as assessed by subsequent competitive transplantation, demonstrating that the *Ptbp1*^{KO} HSC phenotype is not affected by the presence of *Ptbp1*^{KO} cells in the BM microenvironment (Figures S1H and S1I).

Taken together, loss of PTBP1 leads to an increase in immunophenotypically defined BM LT-HSCs and a reduction in HSC self-renewal and their capacity to reconstitute the hematopoietic system.

PTBP1-deficient HSCs display reduced proliferative capacity over time and tend to mobilize spontaneously to the periphery

The functional decline of *Ptbp1*^{KO} HSCs could potentially be due to changes in the cell-fate options normally undertaken by HSCs such as migration, proliferation, differentiation, self-renewal, and survival. We started out by measuring homing, since successful engraftment depends on the capacity of cells to migrate from the PB to the BM. CFSE-labeled, c-kit-enriched BM cells from *Ptbp1*^{KO} and *Ptbp1*$^{fl/fl}$ mice were found to home to the BM and spleen of lethally irradiated recipients with comparable efficiencies in short-term homing experiments (Figure 3A). Furthermore, HSC homing, assayed by competitive repopulation directly following a 3-hour homing window, demonstrated normal homing capacity of *Ptbp1*^{KO} LT-HSCs (Figures S1J–S1L). Although *Ptbp1* deficiency did not affect immediate HSC migration in these assays, we did observe signs of spontaneous HSC mobilization in *Ptbp1*^{KO} mice. Specifically, we detected an increased frequency of immunophenotypically defined HSCs (LSK, CD150$^+$, CD48$^-$) in spleens (Figure 3B) as well as a tendency toward increased colony-forming unit (CFU) formation by cells isolated from the spleen and PB, indicating the presence of circulating progenitors (Figures 3C and 3D).

Increased levels of reactive oxygen species (ROS) have been associated with a decline in HSC function; however, apart from a mild decrease in the MPP4 population in *Ptbp1*^{KO} BM, ROS levels in LT-HSCs, ST-HSCs, MPP2, and MPP3 were similar in *Ptbp1*^{KO} and *Ptbp1*$^{fl/fl}$ mice (Figure 3E). Thus, increased ROS levels do not underlie the functional decline observed in *Ptbp1*^{KO} HSCs.

HSC self-renewal and lineage bias have previously been linked to the levels of certain cell-surface markers including Sca-1 and CD150 (Wilson et al., 2015). In line with the functional decline observed in *Ptbp1*^{KO} HSCs, we noted slightly, but significantly, reduced levels of both Sca-1 and CD150, as measured by the mean fluorescence intensities of these markers, on BM cells previously gated on LT-HSCs (LSK, Flt3$^-$, CD150$^+$, CD48$^-$) (Figures 3F and 3G).

Finally, we assessed HSC proliferation by bromodeoxyuridine (BrdU) incorporation and cell-cycle analysis using Ki67 and DAPI. Three weeks following *Ptbp1* deletion, both assays showed similar numbers of proliferating HSCs in both genotypes (Figures 3H and 3I). However, when the cell-cycle distribution was assessed 4 months after poly-IC treatment, we noted a decrease of HSCs in the G_1 and SG_2M phases, with a corresponding increase in the numbers of quiescent HSCs (G_0) (Figures 3J and 3K). Thus, *Ptbp1*^{KO} HSCs gradually lose their

(G) Overview of competitive repopulation experiment.
(H) PB donor-cell chimerism following competitive repopulation.
(I) PB lineage distribution within the donor-cell compartment 16 weeks posttransplantation.
(J) Donor-cell chimerism within the LSK CD150$^+$ CD48$^-$ compartment 16 weeks posttransplantation.
Error bars indicate SD. Statistical analyses were performed using unpaired, two-tailed Student's t test.
See also Figure S1.

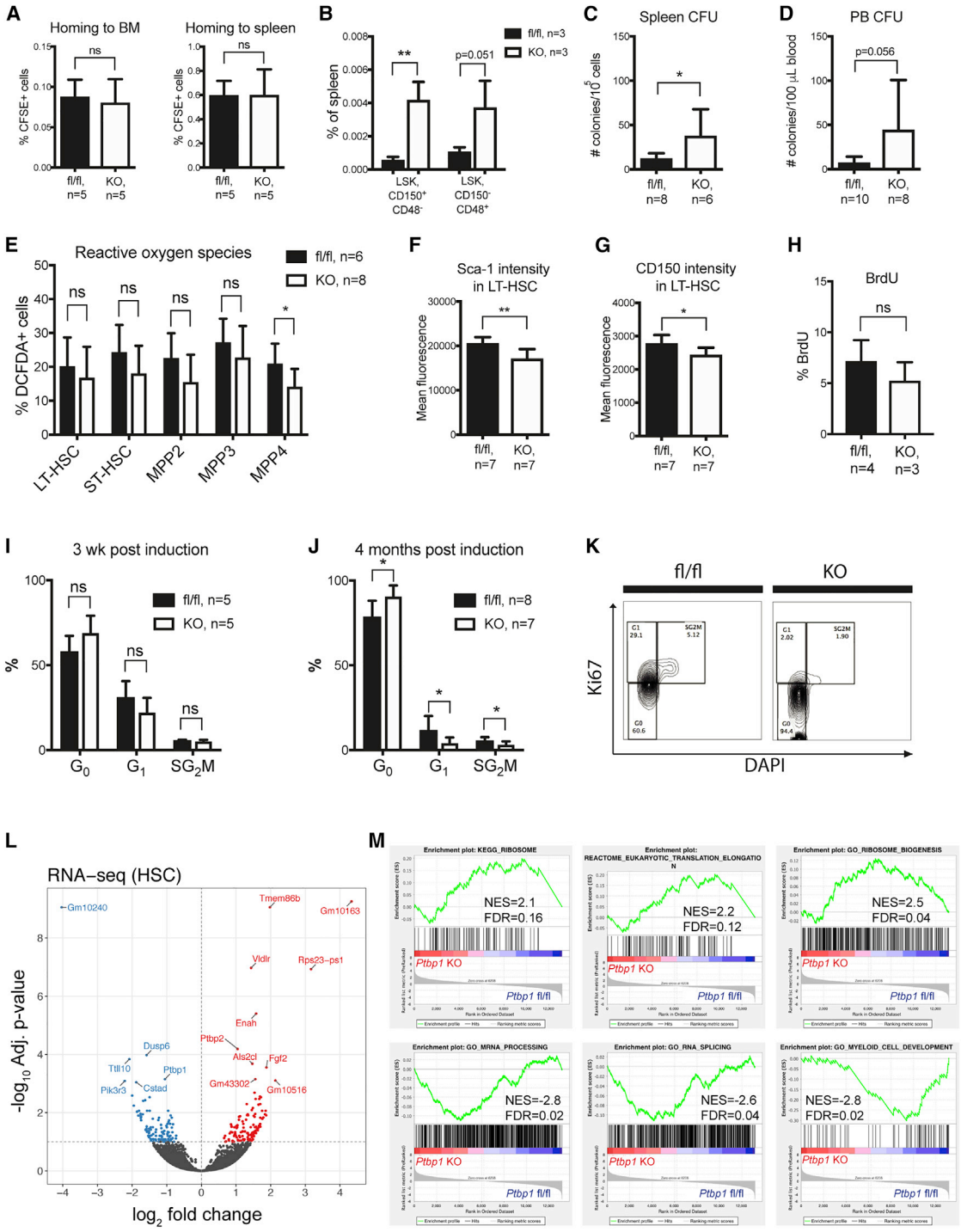

Figure 3. Loss of *Ptbp1* leads to a cell-intrinsic HSC defect and increased HSC quiescence

(A) Frequency of CFSE$^+$ cells in BM and spleen 3 h after injection of 2.5 × 10^6 c-kit$^+$ CFSE-labeled cells per recipients (lethally irradiated).

(B) Spleen HSPCs measured by FACS.

(C) Myeloid colony-forming potential per 1 × 10^5 splenocytes in M3434 medium.

(D) Myeloid colony-forming potential per 100-µL PB seeded in M3434 medium.

(E) Reactive oxygen species (ROS) was measured by DCFDA-labeling.

(F) Mean fluorescence of Sca-1 expression in LT-HSCs from FACS analysis in Figure 2A.

(G) Mean fluorescence of CD150 expression in LT-HSCs from FACS analysis in Figure 2A.

(H) BrdU incorporation in LSK CD150$^+$ CD48$^-$ cells 3 h after injection of BrdU.

(legend continued on next page)

proliferation capacity over time, likely explaining their failure to expand when challenged in a transplantation setting.

In order to identify PTBP1-regulated mRNAs, potentially explaining the observed HSC phenotype in *Ptbp1*^{KO} mice, we performed RNA sequencing (RNA-seq) in purified HSCs (LSK, CD150^{+}, CD48^{-}). This analysis revealed 110 down-regulated and 123 up-regulated genes in *Ptbp1*^{KO} HSCs (DESeq2 adjusted $p \leq 0.1$) (Figure 3L; Table S1). Gene set enrichment analysis (GSEA) demonstrated an enrichment in genes encoding ribosomal constituents among *Ptbp1*^{KO} upregulated genes (Figure 3M; Table S2). Conversely, genes down-regulated in *Ptbp1*^{KO} HSCs were enriched for splicing and differentiation-associated genes (Figure 3M; Table S2).

Taken together, PTBP1-deficient HSCs display several features of reduced HSC fitness.

PTBP1-deficient mice have reduced numbers of erythroid progenitors in the BM

Apart from the functional decline of HSCs, our initial analyses also revealed that loss of PTBP1 was associated with the development of a mild anemia. Further analysis of the myeloid-erythroid compartment (Pronk and Bryder, 2011) (Figure 4A) showed that while the development of myeloid progenitors (pre-granulocytic monocytic progenitor [preGM], granulocytic monocytic progenitor [GMP]) was similar between *Ptbp1*^{KO} and *Ptbp1*$^{fl/fl}$ mice, differentiation toward the megakaryocyte-erythroid lineage is hampered in *Ptbp1*^{KO} BM, resulting in decreased sizes of the pre-megakaryocyte erythroid (preMegE), pre-erythroid colony-forming unit (preCFU-E), and erythroid colony-forming unit (CFU-E) populations (Figures 4A and 4B). Further analyses of erythroid-primed BM cells undergoing terminal differentiation toward RBCs (Liu et al., 2013) demonstrated fewer orthochromatic erythroblasts, reticulocytes, and erythrocytes in *Ptbp1*^{KO} mice, clearly showing that erythropoiesis is impaired in the *Ptbp1*^{KO} setting (Figures 4A and 4C, populations IV–V). This finding was confirmed by a phenylhydrazine challenge experiment where survival following RBC lysis is measured as a proxy for the abundance of erythroid cells and the ability of the BM to induce erythroid output upon stress (Adachi, 1977) (Figure 4D). In line with the observed splenomegaly and the abundance of splenic HSPCs, *Ptbp1*^{KO} mice displayed compensatory extramedullary stress erythropoiesis in the spleen, with increased blast-forming unit-erythroid (BFU-E) colony-forming potential (Figure 4E) and frequencies of terminally differentiating erythroblasts (populations I–V; see Figures 4A and 4F). Stress erythropoiesis can be induced when BM erythroid differentiation is inadequate and is signified by an influx of HSPCs to the spleen (Paulson et al., 2020). This is in line with the increased presence of HSPCs in the periphery of *Ptbp1*^{KO} mice (Figures 3B–3D). Despite the induction of extramedullary erythropoiesis, net erythroid output is not enough to rescue *Ptbp1*^{KO} mice from anemia (Figure 1J–1L). In BM, however, colony-forming assays demonstrated unchanged numbers of both CFUs (mainly assaying myeloid differentiation) and BFU-E (Figures 4G and 4H). We confirmed that the erythroid defect in BM was caused by the cell-intrinsic loss of PTBP1, since BM erythroid development as well as extramedullary hematopoiesis, i.e., spleen size, were normal in *Ptbp1*^{KO} recipients of wild-type BM cells (Figures 4I, 4J, and S1H). Moreover, prospectively isolated CFU-Es exhibited a terminal erythrocyte differentiation defect *in vitro* (erythrocyte differentiation stages RI to RIV) further highlighting the cell-intrinsic nature of the *Ptbp1*^{KO} phenotype (Figures 4K and 4L) (Schneider et al., 2016).

Thus, these analyses established that PTBP1 is indispensable for proper erythropoiesis through a cell intrinsic mechanism(s).

Key erythroid factors are de-regulated in PTBP1-deficient erythroid progenitors

In order to dissect how PTBP1 facilitates efficient erythropoiesis, we performed RNA-seq analysis on preMegEs and preCFU-Es—and identified genes with differential mRNA levels (DESeq2 adjusted $p \leq 0.1$) or splicing events (DEXSeq isoform-switch $q \leq 0.05$) (Figures 5A–5E; Tables S1 and S3). Moreover, as PTBP1 has also been suggested to regulate gene expression by mechanisms downstream of splicing, we performed global proteomics using low-cell-number ($\sim 10^5$ cells/replicate) mass spectrometry (MS) (Schoof et al., 2016). This analysis resulted in the quantification of approximately 5,000 proteins in preMegEs and preCFU-Es, where 180 and 122, respectively, were differentially expressed (absolute log2-fold change >1, Limma $p \leq 0.05$) (Figures 5F and 5G; Table S4).

Splicing changes may potentially affect mRNA abundance, e.g., by alterations of transcript stability, and we did indeed observe that a subset of differentially spliced genes displayed corresponding changes in mRNA levels (Figures 5C and 5D). Other PTBP1-promoted AS events may result in expression of novel protein isoforms. Comparing differentially spliced genes between preMegE and preCFU-E, we noted that only a subset of genes was commonly de-regulated in the two populations (Figure 5E). This demonstrates that although PTBP1 controls certain common genes, most PTBP1-controlled AS occurs in a differentiation stage-specific manner. Global splicing analysis also confirmed a mainly repressive role for PTBP1, since exon skipping (ES) events tended to be increased in *Ptbp1*^{KO} cells, although population-specific differences were noted (Figure S2A). A number of previously identified PTBP1 targets were confirmed, including *Rtn4*, *Ptbp2*, and *Cdc42* (Boutz et al., 2007; He et al., 2015; Makeyev et al., 2007; Yap et al.,

(I) Cell-cycle analysis by Ki67/DAPI in LSK CD150^{+} CD48^{-} HSCs 3 weeks post poly-IC.
(J) Cell-cycle analysis by Ki67/DAPI in LSK CD150^{+} CD48^{-} HSCs 4 months post poly-IC.
(K) Representative FACS plots of cell-cycle analysis by Ki67/DAPI staining in LSK CD150^{+} CD48^{-} HSCs 4 months post poly-IC.
(L) Volcano plot displaying RNA-seq differential expression in HSCs.
(M) GSEA of HSC RNA-seq data.
Error bars indicate SD. Statistical analyses were performed using unpaired, two-tailed Student's t test. CFSE, carboxyfluorescein; CFU, colony-forming unit; DCFDA, 2′,7′-dichlorofluorescein diacetate; BrdU, 5-Bromo-2′-deoxyuridine.
See also Figure S1.

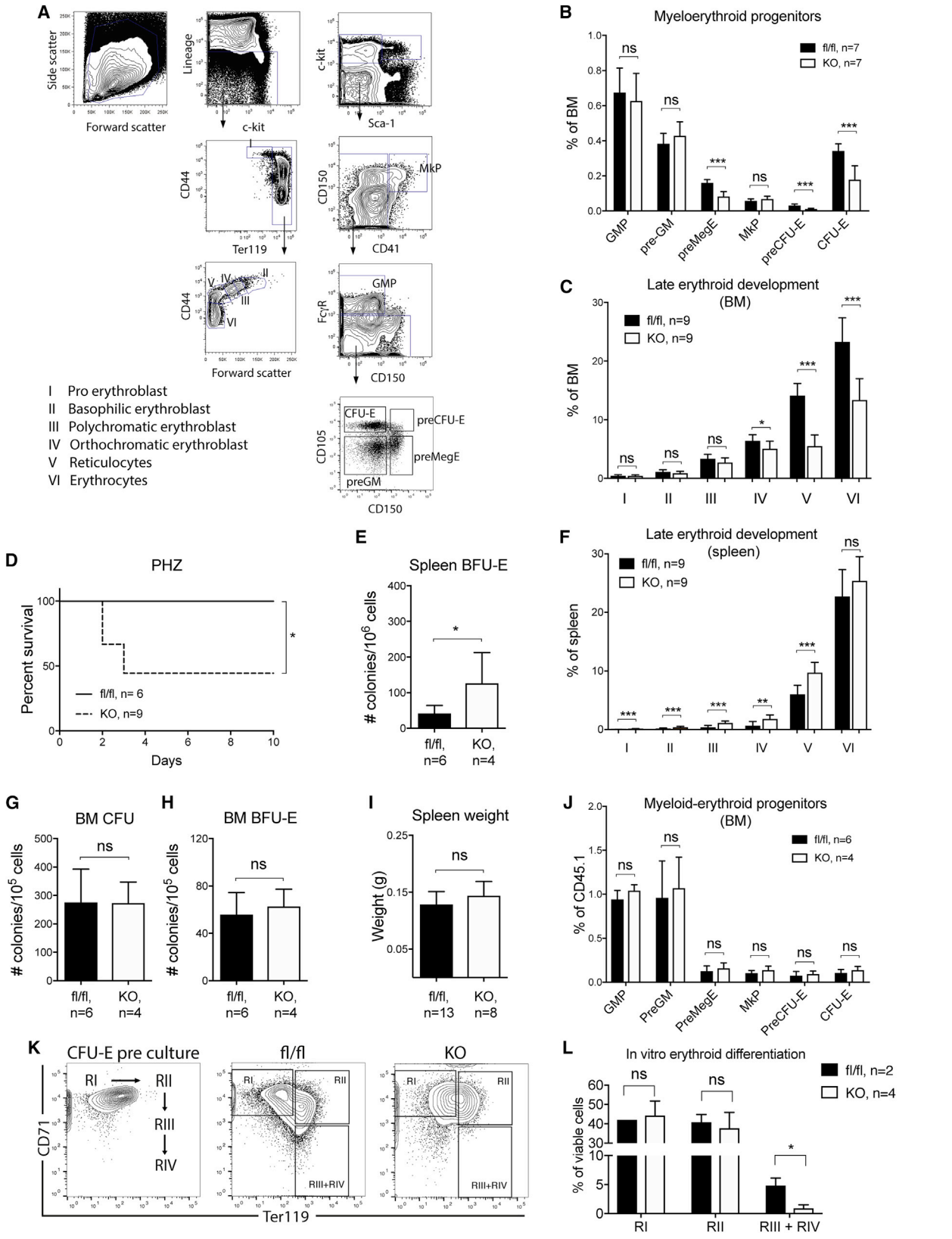

(legend on next page)

2016; Zhang et al., 2016), and these were also verified to be de-regulated at the protein level (Figure S3; Tables S3 and S4; *Cdc42* alternative transcripts discussed below). Finally, in accordance with the HSC transcriptome data, GSEA identified gene sets, including ribosomal proteins and/or genes involved in translational processes, to be up-regulated in *Ptbp1*^{KO} erythroid progenitors, whereas down-regulated genes were enriched within gene sets involved in processing of both ribosomal RNA and mRNA as well as cell proliferation (Figures 5H; Table S2).

Interestingly, when we scrutinized the proteomics data carefully, we detected several differentially expressed proteins disconnected from any apparent changes in mRNA expression or AS. Among these, we noted de-regulated expression of several crucial erythropoietic factors connected to iron homeostasis like hemoglobin (HBA, HBB, AHSP), ferritin (FTH1, FTL1), ATPIF1, and the transferrin receptor (TFRC). Additionally, expression of certain translation-related proteins with reported roles in defective erythropoiesis/BM failure, including RPS14 (Schneider et al., 2016) and EIF2D (Khajuria et al., 2018), were also affected by PTBP1 loss (Figures 5F and 5G). These data clearly demonstrate that changes in transcript levels correlate poorly with changes in protein levels following loss of PTBP1 (Figure 5I). To analyze this more systematically, we focused on the transcriptomic and proteomic datasets generated from preMegE and ranked proteins based on the difference in fold change between mRNA and protein expression into five classes. Classes 1 and 5 represent the two extremes where proteins are down- and up-regulated, respectively, despite minimal or even opposing changes at the transcript levels (Figure 5I). Interestingly, ribosomal proteins (Rps, Rpl) are enriched among the proteins that display the largest discrepancy between mRNA and protein fold changes (class 1), i.e., they are not translated efficiently in the *Ptbp1*^{KO} setting (Figures 5I and 5J). Notably, translation initiation factors (Eif) and mitochondrial ribosomal proteins (Mrp) did not follow the same tendency, in line with the coordinated translational regulation of cytosolic ribosomal proteins (Thoreen et al., 2012) (Figure 5J).

Taken together, these analyses established not only that PTBP1 supports AS in erythropoiesis, mainly in a population-specific manner, but also that protein expression of several key erythroid factors, including ribosomal proteins, is dependent on PTBP1, suggesting that PTBP1 is involved in controlling the translational output of these proteins.

PTBP1-deficient HSCs and erythroid progenitors display a reduced rate of protein synthesis

Ribosomopathies are frequently associated with mutations in ribosomal proteins and are characterized by inefficient erythropoiesis. This is mirrored by mouse models harboring lesions in the corresponding ribosomal proteins, which are further characterized by a decline in HSC function and reduced protein synthesis. Since the HSC and erythroid phenotypes are strikingly similar to those observed in *Ptbp1*^{KO} mice, it prompted us to investigate protein synthesis rates in *Ptbp1*^{KO} BM using O-propargyl-puromycin (OP-puro). Strikingly, protein-synthesis rates in *Ptbp1*^{KO} cells were decreased by 10%–30% in most BM populations analyzed (Figures 6A–6C), which clearly established that PTBP1 is required for efficient protein synthesis throughout hematopoiesis.

We scrutinized further our RNA-seq datasets in order to identify differentially expressed PTBP1-controlled splice variants that might affect protein translation and/or ribosomal biogenesis. Given that protein synthesis is decreased in HSCs and erythroid cells (and seemingly most other cell types in the BM), we looked for differentially spliced genes that were commonly de-regulated in all the three RNA-seq datasets generated (HSCs, preMegEs, and preCFU-Es). We identified 27 genes where a lack of PTBP1 leads to differential splicing, common between all three populations analyzed (DEXSeq isoform switch q $\leq$ 0.1) (Figure 6D). Notably, CDC42 isoforms have been shown to differentially impact activation of the p70-S6-kinase (Chou and Blenis, 1996), a rate-limiting step in translational initiation. Indeed, the splicing event controlling the balance between *Cdc42* isoforms 1 (*Cdc42*-1) and 2 (*Cdc42*-2) is dependent on PTBP1 (He et al., 2015; Yap et al., 2016), and thus, upon PTBP1 deficiency, *Cdc42*-2 is upregulated in HSCs, preMegEs, and preCFU-Es (Figures 6E and 6F). Furthermore, the up-regulation of CDC42-2 was also confirmed at the protein level, evident by MS-based protein quantification in preMegEs and preCFU-Es (Figure 6G). Given that CDC42-2 is the more p70-S6K inhibitory isoform, we hypothesized that the gain of this isoform in *Ptbp1*^{KO}

Figure 4. *Ptbp1*-deficient mice have reduced numbers of erythroid progenitors in the BM

(A) Overview of FACS strategy used to discern myeloid-erythroid development (Liu et al., 2013; Pronk and Bryder, 2011).
(B) Frequencies of myeloid-erythroid progenitors in BM; quantification of FACS analysis in (A).
(C) Frequencies of terminally differentiating erythroblasts in BM; quantification of FACS analysis in (A).
(D) Survival following phenylhydrazine (PHZ) challenge.
(E) BFU-E potential from splenocytes seeded in M3436 medium.
(F) Frequencies of terminally differentiating erythroblasts in spleen.
(G) Myeloid colony-forming potential from BM cells seeded in M3434 medium.
(H) BFU-E potential from BM cells seeded in M3436 medium.
(I) Spleen weight in *Ptbp1*$^{fl/fl}$ and *Ptbp1*^{KO} recipients, reconstituted with wild-type BM cells 4 months earlier.
(J) Frequencies of myeloid-erythroid progenitors within the donor-cell compartment of *Ptbp1*$^{fl/fl}$ and *Ptbp1*^{KO} recipients, reconstituted with wild-type BM cells (CD45.1) 4 months earlier.
(K) Representative FACS plots and gating strategy before and after *in vitro* differentiation cultures of sorted CFU-Es.
(L) Quantification of erythroid differentiation stages 6 days after induction of erythroid differentiation of sorted CFU-Es.
Error bars indicate SD. Statistical analyses were performed using unpaired, two-tailed Student's t test. BFU-E, blast-forming unit erythroid; CFU, colony-forming unit.
See also Figure S1.

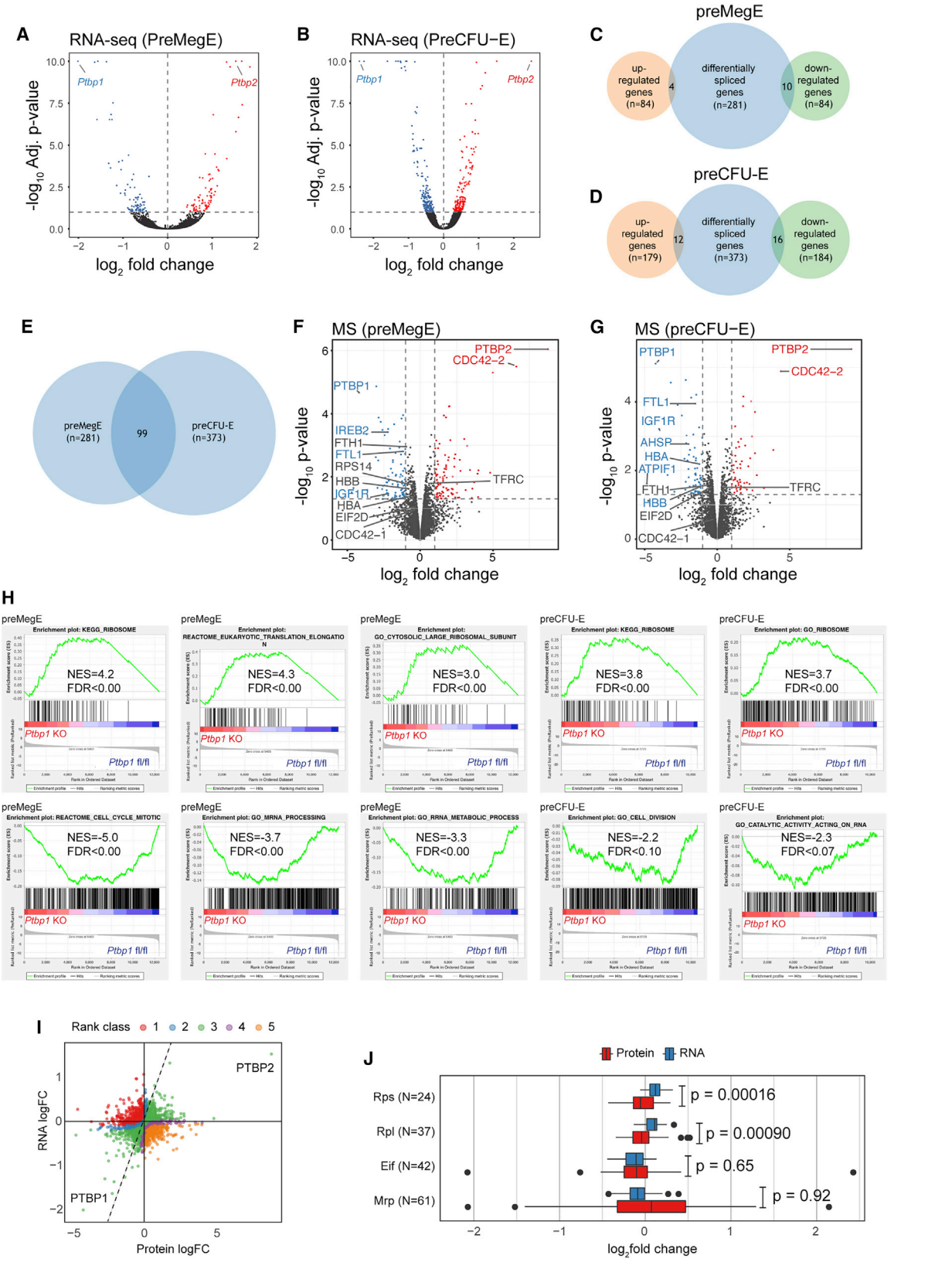

(legend on next page)

cells could be responsible for the observed down-regulation of protein synthesis. To test this, we retrovirally overexpressed the two CDC42 isoforms in wild-type HSPCs and investigated whether the overexpression of *Cdc42*-2 would mimic the *Ptbp1*^{KO} protein-synthesis defect. Following verification of CDC42 isoform overexpression by MS (Figure 6H), we subsequently transplanted *Cdc42*-1- and *Cdc42*-2-transduced cells into lethally irradiated mice. Following an engraftment period of 4 weeks, we measured the abundance of Ter119^{+} cells and protein synthesis rates in transduced erythroid cells. While the frequencies of transduced Ter119^{+} cells were unaltered across the experimental conditions (Figure 6I), OP-puro incorporation was significantly reduced in *Cdc42*-2-overexpressing cells, suggesting a dominant negative effect of this isoform on protein synthesis (Figure 6J).

Additionally, the insulin-like growth factor 1 receptor (IGF1R), which also acts upstream of mTOR, was investigated as another potential mediator of the protein-synthesis deficiency in *Ptbp1*^{KO} mice, as we noted distinct down-regulation of this protein in both preMegEs and preCFU-Es (Figures 5F and 5G). However, OP-puro *in vivo* analysis of recipients of *Igf1r*$^{+/-}$ BM cells did not mimic the results seen in *Ptbp1*^{KO} mice (Figure 6K).

In summary, PTBP1 deficiency is associated with a reduction in protein-synthesis rates in hematopoietic cells, which could be partly mimicked by overexpression of the CDC42-2 isoform normally repressed by PTBP1.

Loss of PTBP1 is associated with defects in pre-rRNA processing

In addition to its effects on *Cdc42* pre-mRNA splicing, our data suggested that PTBP1 might also impact protein synthesis by other means, and we therefore started to explore alternative mechanisms. First, to exclude that the decline in protein synthesis following loss of PTBP1 was due to an overall decrease in cellular metabolism, we measured RNA synthesis rates in HSPCs cells using 5-ethynyl-uridine (5-EU) but found no differences between the *Ptbp1*$^{fl/fl}$ and *Ptbp1*^{KO} genotypes (Figure 7A). Despite normal RNA synthesis, total cellular RNA levels of *Ptbp1*^{KO} Ter119^{+} erythrocytes and LSK were reduced due to a decline in ribosomal RNA, which normally constitutes 85% of cellular RNA content (Figures 7B and S4A). These observations suggest that while pre-rRNA synthesis is normal in *Ptbp1*^{KO} mice, its processing toward mature rRNA might be hampered.

To investigate posttranscriptional steps in pre-rRNA processing (Figure 7C), we quantified ratios of different processing intermediates in Ter119^{+} cells using northern-blot analysis (Figure 7D) (Wang et al., 2014). Although no significant changes were observed in the generation of several major rRNA precursors (20S, 32S, 12S pre-rRNAs), the analysis revealed a marked increase in the 34S/36S pre-rRNA ratio (Figure 7E) following loss of PTBP1. The increased 34S/36S ratio was also evident when the 34S and 36S were quantified against the primary transcript plus (PTP), which contains the large co-migrating 47S, 46S, and 45S pre-rRNAs (Figure 7E). This indicates that while the *Ptbp1*^{KO} cells are not generally impaired in ribosome assembly, the assembly rates for the two subunits are not perfectly balanced, resulting in altered kinetics of the two internal transcribed spacer 1 (ITS1) cleavages (termed 2b and 2c in murine cells) (Figure 7C). Moreover, this defect was accompanied by a strong accumulation of small pre-rRNA ITS fragments in *Ptbp1*^{KO} Ter119^{+} cells and unfractionated BM, suggesting that their normal decay is hampered (Figures 7D, 7F, S4B, and S4C). Indeed, publicly available PTBP1 CLIP data (available through ENCODE, eCLIP in K562 cells) (Van Nostrand et al., 2020) are consistent with PTBP1 directly binding within the ITS1 region in cells of hematopoietic origin (Figure S4D).

Collectively, these analyses suggest that PTBP1 is required for efficient processing of pre-rRNA transcripts.

Transcripts encoding ribosomal proteins are preferentially bound by PTBP1

We next wanted to understand the mechanistic basis of why the translational output of some transcripts was particularly sensitive to loss of PTBP1 (Figure 5I). Interestingly, PTBP1 is a known regulator of the translational output of IRES-containing transcripts, which are characterized by their high pyrimidine content. Moreover, PTBP1 has been suggested to be involved in translational regulation of ribosomal proteins (Pichon et al., 2012), and their corresponding transcripts are known to be under control of the pyrimidine-rich TOP motif. Given these data, we explored features of 5′ UTRs of the different transcript classes. While the overall length and pyrimidine composition were similar between the five transcript classes, we noticed that transcripts encoding ribosomal proteins displayed a higher pyrimidine content (Figures 7G–7I). Using available PTBP1 CLIP-seq datasets, we found that PTBP1/PTBP2 (a close homologue) binding peaks (Vuong et al., 2016) or motifs identified through cross-linking experiments (Xue et al., 2009) were significantly enriched in 5′ UTRs of class 1 and 2 transcripts compared with class 4 and 5 (Figure 7J). This indicates that transcripts associated with decreased translation upon PTBP1 loss do indeed have more binding of PTBP1 in their 5′ UTRs in the normal setting.

Figure 5. Transcriptional, splicing, and proteomic analyses of *Ptbp1*$^{fl/fl}$ and *Ptbp1*^{KO} preMegEs and preCFU-Es

(A and B) Volcano plot displaying RNA-seq differential expression in (A) preMegEs and (B) preCFU-Es.

(C and D) Overlaps between differentially expressed genes and differentially spliced genes determined by DESeq2 and DEXSeq analysis in (C) preMegEs and (D) preCFU-Es.

(E) Differentially spliced genes in common between preMegEs and preCFU-Es.

(F and G) Volcano plot displaying differentially expressed proteins in (F) preMegE and (G) preCFU-E, analyzed by MS.

(H) GSEA of RNA-seq data from preMegEs and preCFU-Es.

(I) preMegE mRNA and protein log2 fold changes, colored by rank class.

(J) mRNA and protein log2 fold changes in the different protein classes.

Boxes indicate the interquartile range (IQR), thick bar indicates the median, whiskers extend to values within 1.5 times the IQR, and dots depict outliers. Statistical significance was determined by one-sided Wilcoxon signed-rank test.

See also Figures S2 and S3.

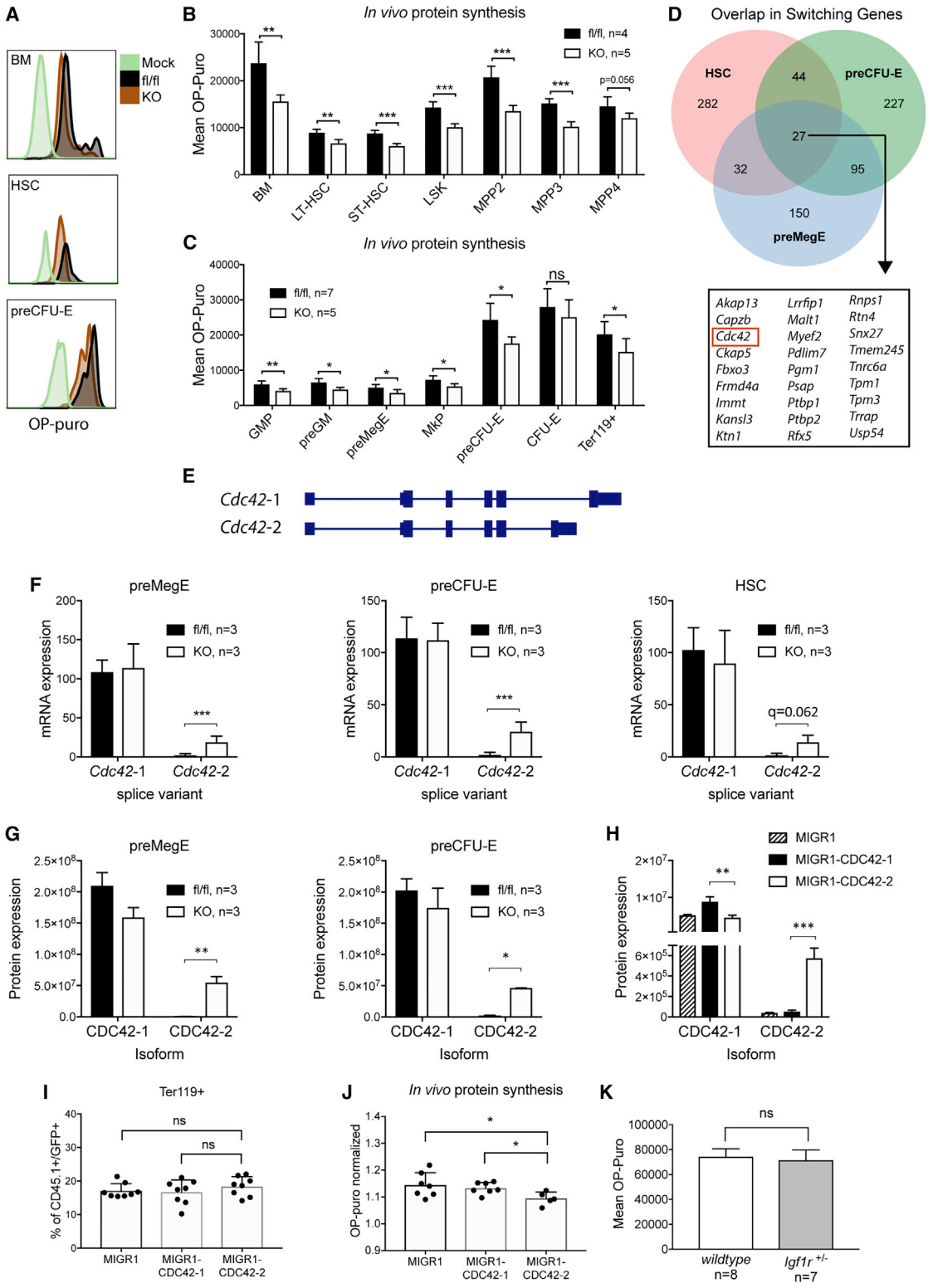

Figure 6. *Ptbp1* deficiency causes protein-synthesis perturbations that can be partly mimicked by CDC42 isoform 2 overexpression

(A) Representative FACS profiles of OP-puro analysis.

(B) *In vivo* protein-synthesis rates in BM HSPCs.

(C) *In vivo* protein-synthesis rates in BM myeloid-erythroid progenitors.

(legend continued on next page)

Enrichment of PTBP1 binding in class 1 and 2 transcripts was also confirmed by enrichment of motifs identified via *in vitro* RNA-binding assays (Ray et al., 2013) (Figure 7J). Finally, publicly available global analyses of RNA binding in K562 cells (Budak et al., 2017; Van Nostrand et al., 2020) revealed that PTBP1 binding was highly enriched in transcripts encoding factors involved in translation including the Gene Ontology categories "cytosolic small ribosomal subunit" and "cytosolic large ribosomal subunit" (Figure S5A; Table S5).

Finally, we investigated the distribution of certain motifs known to control translational output (Eliseeva et al., 2013; Hsieh et al., 2012) between the different transcript classes. Here, we demonstrated that the pyrimidine-rich translational element (PRTE), TOP (Hsieh et al., 2012), as well as the OP (Eliseeva et al., 2013) motif as defined by Eliseeva et al. were more abundant in 5′ UTRs of class 1 and 2 transcripts. Similarly, the PRTE and TOP motifs were enriched in ribosomal-protein transcripts compared with mRNAs of the remaining expressed proteins in this dataset (Figures 5I and 7K). When focusing specifically on ribosomal proteins, the presence of the PRTE or OP motif could in fact predict their down-regulation at the protein level within our dataset (Figures 7L and 7M).

In summary, these analyses suggest that PTBP1 binding to 5′ UTR is necessary to maintain proper translation levels of certain proteins, in particular proteins related to the translational machinery itself.

DISCUSSION

Ribosomopathies are a collection of congenital disorders affecting the structure and/or function of ribosomal components, and studies in patients and murine models have shown that these diseases are associated with anemia and a decline in HSC function. In this work, we found that loss of PTBP1 resulted in HSC functional defects and impaired erythroid development and, furthermore, demonstrated that PTBP1 is necessary for maintaining efficient protein synthesis in BM cells. Our findings support previous reports underlining the role of protein synthesis in developmental biology (Blanco et al., 2016; Corsini et al., 2018; Signer et al., 2014; Tahmasebi et al., 2018) and the fact that the HSC compartment and erythroid lineage are highly sensitive to perturbations in protein synthesis (Jaako et al., 2011; Schneider et al., 2016). In summary, loss of PTBP1 in murine hematopoiesis leads to a ribosomopathy-like condition.

As for the LT-HSCs, this compartment is slightly enlarged in *Ptbp1*^{KO} mice, while their ability to sustain hematopoietic reconstitution is reduced. Whereas this dysfunction is not initially connected to a reduction in proliferation, the numbers of proliferating HSCs decrease over time in the absence of PTBP1, indicating a progressive functional decline of the HSC compartment. Consistently, it has previously been shown that reduced protein-synthesis rates in HSCs leads to functional loss, irrespective of their cycling status (Signer et al., 2014).

Loss of PTBP1 also results in aberrant differentiation of erythroid cells, with decreased fractions of erythroid progenitor cells in the BM and reduced numbers of mature RBCs in the periphery. This differentiation defect is likely caused by the reduced protein-synthesis rates in these cells and, similar to the HSC compartment, is not connected initially to an overall decrease in proliferation, findings that are also consistent with RNA synthesis rates remaining at normal levels in *Ptbp1*^{KO} HSPCs.

Our data suggest that the impact of PTBP1 loss on protein synthesis appears to be governed by multiple mechanisms, all impinging on the generation of functional ribosomes. These include (1) altered splicing of CDC42, a factor reported to be important for translational initiation, (2) efficient translation of ribosomal proteins, and (3) efficient processing of pre-rRNA. Thus, PTBP1 appears as a crucial regulator of ribosome biogenesis.

In line with its *bona fide* role as a splicing regulator, splicing patterns are altered in *Ptbp1*^{KO} BM cells, and we confirm several published targets where the balances between different isoforms are changed. By comparing our RNA-seq datasets generated from HSCs, preMegEs, and preCFU-Es, it is evident that splicing events controlled by PTBP1 are largely differentiation-stage specific, as we find only minor overlapping differential splicing events between the three populations. Among these, we observe up-regulation of the CDC42-2 isoform at both transcript and protein levels and demonstrate that its overexpression leads to a mild reduction in protein synthesis *in vivo* but does not affect the number of erythroid cells. Apart from *Cdc42*, there is an apparent lack of splicing targets connected to protein synthesis in our dataset, suggesting that de-regulation of AS is only partly responsible for the protein-synthesis phenotype observed in *Ptbp1*^{KO} cells.

We find that genes encoding ribosomal proteins belong to a class of transcripts that display anti-correlative changes in mRNA and protein levels following loss of PTBP1 in erythroid

(D) Common PTBP1 regulated AS between HSCs, preMegEs, and preCFU-Es.
(E) *Cdc42* transcript splice variants (*Cdc42*-1, NCBI: NM_009861.3; *Cdc42*-2, NCBI: NM_001243769.1).
(F) *Cdc42* transcript splice variant expression in HSCs, preMegEs, and preCFU-Es. Error bars indicate standard error. Statistical analysis by DEXSeq isoform switch tool. A third *Cdc42* splice variant was identified by DEXseq2 (data not shown), with unchanged expression between the genotypes, giving rise to a protein isoform identical to CDC42-1.
(G) CDC42 protein isoform expression in preMegEs and preCFU-Es (CDC42-1, Uniprot: P0766; CDC42-2, Uniprot: P0766-1) as determined by MS. Statistical analysis by Limma differential expression analysis.
(H) CDC42 protein isoform expression in GFP$^+$ retrovirally transduced HSPCs, n = 4.
(I) Percentage of Ter119$^+$ cells within BM cells gated on CD45.1$^+$/GFP$^+$ in recipient mice of CDC42 isoform transduced cells.
(J) OP-puro *in vivo* analysis in CDC42 isoform transplanted recipients. Data are represented as mean OP-puro incorporation in Ter119$^+$/GFP$^+$ cells, normalized to OP-puro incorporation in Ter119$^+$/GFP$^-$ cells within each sample.
(K) *In vivo* protein-synthesis rates in Ter119$^+$ cells in recipients of wild-type control and *Igf1r*$^{+/-}$ BM cells 4 weeks after BM transplant.
Error bars indicate SD if not stated otherwise. Statistical analyses were performed using unpaired, two-tailed Student's t test if not stated otherwise. OP-puro, O-propargyl-puromycin.

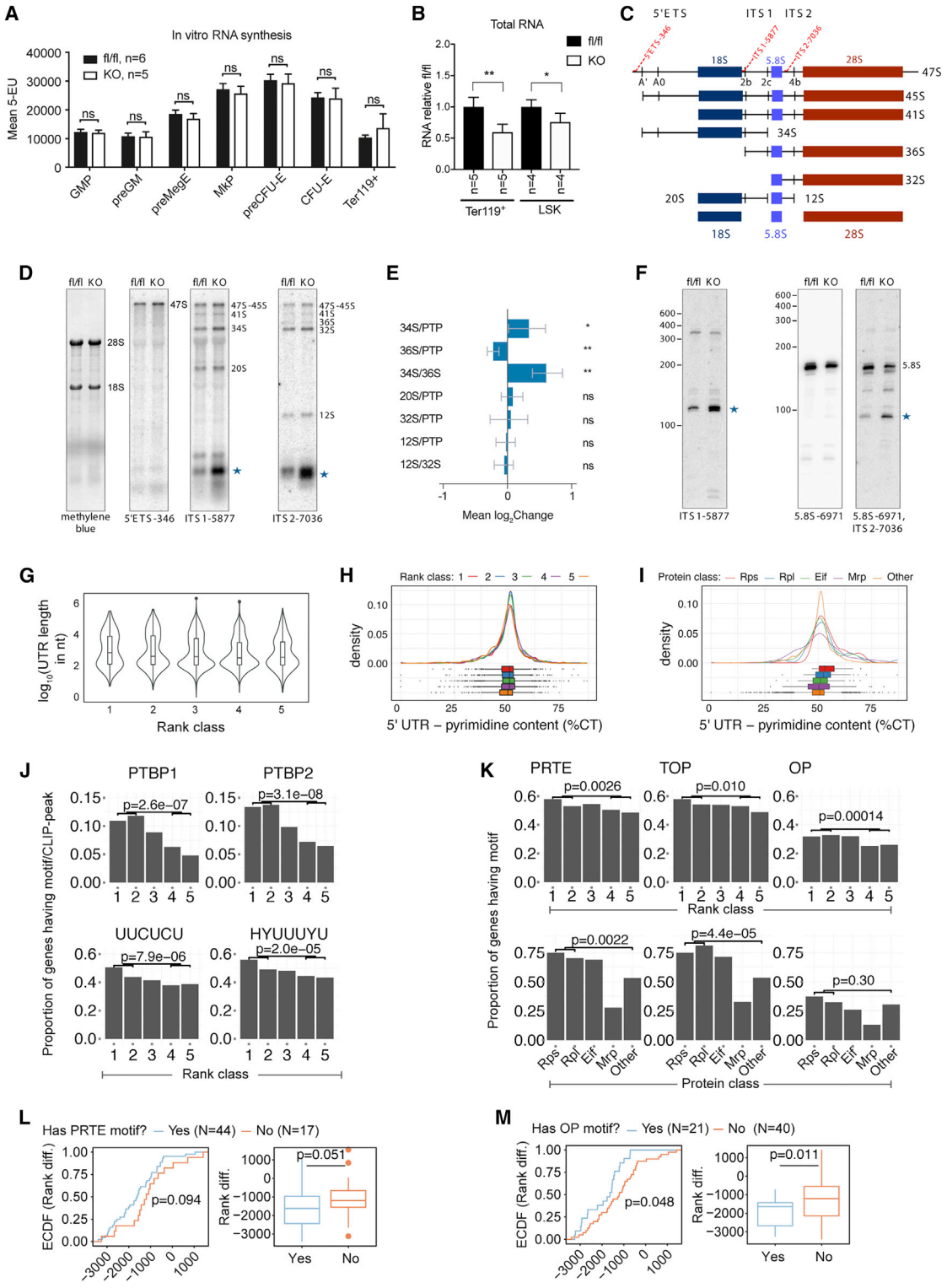

Figure 7. Effects on ribosomal RNA processing and 5′ UTR analysis of mRNAs sensitive to translational regulation in *Ptbp1* deficient cells

(A) *In vitro* RNA synthesis rates measured by 5-EU incorporation in BM myeloid-erythroid progenitors.

(B) Total RNA obtained from 5 × 10^6 Ter119$^+$ cells or 7 × 10^4 LSK cells, respectively. Values are normalized to *Ptbp1*$^{fl/fl}$ for each cell type.

(C) Schematic overview of major rRNA precursors in murine cells.

(legend continued on next page)

progenitor cells. Apart from highlighting the importance of using protein data, these findings strongly suggest that loss of PTBP1 alters the translational output of a subset of mRNAs. *Cis*-acting elements controlling translational output of ribosomal proteins, such as the TOP motif, have been well-studied (Meyuhas and Kahan, 2015). However, relatively few *trans*-acting proteins that control the translational output of TOP-containing transcripts have been identified, and most of these restrict translational output upon binding as a means of limiting protein synthesis in situations of poor nutrient availability (Nandagopal and Roux, 2015). We show that class 1 transcripts are enriched for PTBP1 binding, as determined by CLIP experiments, and for pyrimidine motifs previously shown to control translational output of their respective transcripts. Although binding of PTBP1 to these motifs has not previously been shown, our data suggest that PTBP1 associates with pyrimidine-rich sequences in 5′ UTRs of selected transcripts, thereby affecting their protein-expression levels. Indeed, PTBP1 has previously been demonstrated to bind to a pyrimidine-rich sequence in the murine *Rpl32* 5′ UTR (Severson et al., 1995), and a 57-kD protein (equals the size of PTBP1) was shown to bind the 5′ UTR of Xenopus *rpl1* mRNA (Cardinali et al., 1993). Moreover, PTBP1 has been reported to increase the translational efficiency of the *FLT3*mRNA in AML (Sun et al., 2019) and was also identified in a proteomics screen for proteins binding to 5′-cap structures of TOP transcripts following insulin-mediated stimulation of protein synthesis. Interestingly, this screen identified several other hnRNPs belonging to the same family of splice factors as PTBP1, and it was argued that their nuclear-cytoplasmic-shuttling properties may be key in determining selective translation of certain mRNAs (Tcherkezian et al., 2014). Collectively, these findings provide ample evidence for the ability of PTBP1 to interact with 5′ UTRs as a means of regulating translation of selected transcripts. Moreover, the splicing factor U2AF1 has also been shown to repress translational output of certain mRNAs through binding to pyrimidine-rich regions in 5′ UTRs (Palangat et al., 2019). Similar to what we describe here, an altered function of U2AF1, as seen in patients with mutations in this gene, affects hematopoietic differentiation resulting in MDS. Thus the role of splicing factors in governing RNA metabolism is clearly extending beyond merely the regulation of splicing events.

Finally, our data also support a role for PTBP1 in the multistep process of ribosome assembly. Specifically, we show that *Ptbp1*^{KO} Ter119^{+} erythroid cells display imbalances in the two ITS1 cleavages that split the pre-rRNA transcript to separate the small and large subunit pre-rRNA species during their maturation. Concordant with our observations, an increase in a 5.8S rRNA-proximal cleavage in ITS1 relative to the 18S-proximal one was previously shown to correlate with reduced growth-factor signaling and reduced small subunit assembly kinetics in murine fibroblasts (Wang et al., 2014). A similar switch was observed in response to stress and nutrient depletion in yeast (Kos-Braun et al., 2017). Further, we speculate that the abnormal ITS fragment accumulation in *Ptbp1*^{KO} Ter119^{+} erythroid cells could lead to further detrimental effects on ribosome assembly. Potentially, the accumulated fragments might activate signaling responses and/or retain ITS binding factors, thus preventing their recycling for the next rounds of assembly. The extent to which PTBP1 plays a direct role in pre-RNA processing and ribosome assembly is not clear. While CLIP data do suggest an interaction between PTBP1 and pre-rRNA ITS1, it is also well-known that haploinsufficiency of individual ribosomal proteins (e.g., RPS14; RPS19) leads to pre-RNA processing phenotypes. Thus, the reduced availability of ribosomal proteins that we observe in *Ptbp1*^{KO} cells may likely feed back into ribosome assembly, further highlighting PTBP1 as a key integrator of the availability of ribosome constituents.

As of now, PTBP1 lesions have not been associated with ribosomopathy in humans. Here, we circumvented the early embryonic lethality of homozygous *Ptbp1* loss using tissue-specific Cre deletion, which led to a relatively mild form of anemia. Thus, we suspect that a near-complete loss of PTBP1 function

(D) Total RNA from Ter119^{+} cells separated in 1% agarose-formaldehyde gels was transferred to nylon membranes. Mature 28S and 18S rRNAs were visualized by methylene blue staining, and rRNA precursors were detected by northern hybridizations with probes indicated at the bottom. Representative images are shown. Asterisks indicate excised ITS fragments.

(E) Ratio analysis of pre-rRNAs from (D) (Wang et al., 2014) in *Ptbp1*^{KO} (n = 8) relative to the corresponding ratios in *Ptbp1*$^{fl/fl}$ (n = 5); significance was determined using two-way ANOVA with the Tukey post test. Primary transcript plus (PTP) refers to the comigrating 47S, 46S, and 45S pre-rRNAs.

(F) Northern hybridizations (total RNA from Ter119^{+} cells) of the small rRNA fragments separated on 8% polyacrylamide-urea gels with probes indicated at the bottom; molecular sizes in nt (left) are derived from an RNA marker loaded on the same gel.

(G) 5′ UTR length of class 1–5 mRNAs.

(H) 5′ UTR pyrimidine content of class 1–5 mRNAs. Boxes indicate the IQR, thick bar indicates the median, and whiskers extend to values within 1.5 times the IQR.

(I) 5′ UTR pyrimidine content of indicated protein classes. Boxes indicate the IQR, thick bar indicates the median, and whiskers extend to values within 1.5 times the IQR.

(J) PTBP1 and PTBP2 CLIP peaks in 5′ UTRs of class 1–5 mRNAs (top panel) and indicated PTBP1 binding motifs in 5′ UTRs of class 1–5 mRNAs (bottom panel). Statistical significance was determined by one-sided Fisher's exact test, testing for an odds ratio greater than one.

(K) Presence of indicated translation-regulatory motifs in 5′ UTRs of class 1–5 mRNAs (top panel) or in indicated protein classes (bottom panel). Statistical significance was determined by one-sided Fisher's exact test, testing for an odds ratio greater than one.

(L and M) Presence of the (L) PRTE and (M) OP motifs (any of primary, broad, narrow) in ribosomal proteins (Rps and Rpl combined). Left: empirical cumulative distribution function (ECDF) of rank differences. Statistical significance was determined by one-sided Kolmogorov Smirnov test. Right: boxplot of the rank differences. Boxes indicate the IQR, thick bar indicates the median, whiskers extend to values within 1.5 times the IQR, and dots depict outliers.

Statistical significance was determined by one-sided Mann-Whitney test. Error bars indicate SD if not stated otherwise. Statistical analyses were performed using unpaired, two-tailed Student's t test if not stated otherwise. 5-EU, 5-ethynyl-uridine; ITS, internal transcribed spacer; ETS, external transcribed spacer; PRTE, pyrimidine-rich translational element; TOP, terminal oligopyrimidine tract; OP, oligopyrimidine tract.

See also Figures S4 and S5 and Table S6.

would be required for the development of human ribosomopathy and that such embryos are lost early in development. We also note that inactivation of *Ptbp1* is associated with the corresponding up-regulation of its paralog *Ptbp2* via the de-repression of a splicing event that is associated with the generation of a functional *Ptbp2* transcript (Spellman et al., 2007). As PTBP2 displays overlapping binding sites to those observed for PTBP1, the phenotype that we do observe might even be partially masked by the upregulation of PTBP2.

In summary, we have shown that the hematopoietic-specific loss of PTBP1 results in the development of phenotypes mimicking those observed in human ribosomopathies. Thus, based on our findings, we propose that PTBP1 acts as an integrator for the efficient production of ribosomal constituents, not only by its canonical role in pre-mRNA splicing but also through its ability to control ribosomal protein levels and ribosomal particle assembly via non-splicing associated mechanism(s). More broadly, our data highlight the increasing recognition of the importance of RBPs in normal development and in disease and emphasize the need to address their potential non-canonical functions.

Limitations of the study

While our findings clearly reveal an important role of PTBP1 as an integrator of protein synthesis in hematopoietic cells, it is currently not clear whether this extends to other cell types beyond the hematopoietic system. Similarly, it remains to be determined if loss of PTBP1 in human hematopoiesis leads to ribosompathy-like conditions. Finally, the precise mechanistic details as to how PTBP1 modulates rRNA processing, ribosome assembly, and translation of selected transcripts also remain questions to address in future studies.

STAR★METHODS

Detailed methods are provided in the online version of this paper and include the following:

- KEY RESOURCES TABLE
- RESOURCE AVAILABILITY
  - Lead contact
  - Materials availability
  - Data and code availability
- EXPERIMENTAL MODEL AND SUBJECT DETAILS
- METHOD DETAILS
  - Genotyping
  - Transplantations
  - Homing assays
  - Phenylhydrazine treatment
  - Colony assays
  - Peripheral blood analysis by hematocytometry
  - Histology
  - Flow cytometry
  - Terminal erythroid differentiation *in vitro* assay
  - *In vivo* protein synthesis analysis in BM chimeras
  - RNA-seq
  - Global proteomics analysis
  - Northern blot and rRNA transcript analysis
- QUANTIFICATION AND STATISTICAL ANALYSIS
  - RNA-seq differential expression analysis
  - Differential splicing analysis
  - Label-free quantitative proteomics analysis
  - Analysis of the preMegE transcriptome vs. proteome
  - PTBP1 CLIP data and binding motif analysis
  - Mapping of K562 eCLIP data to the human rDNA sequence
  - Seten

SUPPLEMENTAL INFORMATION

Supplemental information can be found online at https://doi.org/10.1016/j.celrep.2022.110793.

ACKNOWLEDGMENTS

This work was supported by grants from the Lundbeck Foundation (2011-9299, R140-2013-13240), the Swedish Childhood Cancer Fund (Barncancerfonden TJ2014-0027), and the Novo Nordisk Foundation (NNF16OC0022330 and NNF17OC0028278) and through a grant from the Novo Nordisk Foundation (Novo Nordisk Foundation Center for Stem Cell Biology, DanStem; grant number NNF17CC0027852). We thank Anna Fossum, Anne Møller, Inge Damgaard, and Lotte Ankjær for technical help, Chirag Nepal for suggestions in TOP-motif analysis, and members of the Porse lab for discussions.

AUTHOR CONTRIBUTIONS

Conceptualization, M.R., D.G.P., and B.T.P.; formal analysis, A.W., S.P., K.V.-S., M.M., N.R., E.M.S., and D.G.P.; investigation, M.R., A.W., S.P., N.J., A.-K.F., Y.G., M.B.S., J.J., E.M.S., T.L.J., R.T.S., and K.L.A.; resources, M.S. and M.H.; writing – original draft, M.R. and B.T.P.; writing – review & editing, M.R. and B.T.P.; visualization, M.R., A.W., S.P., D.G.P., and K.V.-S.; supervision, B.T.P., D.G.P., and A.H.L.; funding acquisition, M.R. and B.T.P.

DECLARATION OF INTERESTS

The authors declare no competing interests.

Received: June 7, 2021
Revised: March 14, 2022
Accepted: April 15, 2022
Published: May 10, 2022

REFERENCES

Adachi, H. (1977). Pathological study on experimental Heinz body anemia: intracellular changes of phagocytized red cells in macrophages of the spleen and liver. Acta Pathol. Jpn. *27*, 657–675. https://doi.org/10.1111/j.1440-1827.1977.tb00184.x.

Anders, S., Reyes, A., and Huber, W. (2012). Detecting differential usage of exons from RNA-seq data. Genome Res. *22*, 2008–2017. https://doi.org/10.1101/gr.133744.111.

Baralle, F.E., and Giudice, J. (2017). Alternative splicing as a regulator of development and tissue identity. Nat. Rev. Mol. Cell Biol. *18*, 437–451. https://doi.org/10.1038/nrm.2017.27.

Bielli, P., Panzeri, V., Lattanzio, R., Mutascio, S., Pieraccioli, M., Volpe, E., Pagliarulo, V., Piantelli, M., Giannantoni, A., Di Stasi, S.M., and Sette, C. (2018). The splicing factor PTBP1 promotes expression of oncogenic splice variants and predicts poor prognosis in patients with non-muscle-invasive bladder cancer. Clin. Cancer. Res. *24*, 5422–5432. https://doi.org/10.1158/1078-0432.ccr-17-3850.

Blanco, S., Bandiera, R., Popis, M., Hussain, S., Lombard, P., Aleksic, J., Sajini, A., Tanna, H., Cortes-Garrido, R., Gkatza, N., et al. (2016). Stem cell

function and stress response are controlled by protein synthesis. Nature *534*, 335–340. https://doi.org/10.1038/nature18282.

Boutz, P.L., Stoilov, P., Li, Q., Lin, C.H., Chawla, G., Ostrow, K., Shiue, L., Ares, M., Jr., and Black, D.L. (2007). A post-transcriptional regulatory switch in polypyrimidine tract-binding proteins reprograms alternative splicing in developing neurons. Genes Dev. *21*, 1636–1652. https://doi.org/10.1101/gad.1558107.

Brinegar, A.E., and Cooper, T.A. (2016). Roles for RNA-binding proteins in development and disease. Brain. Res. *1647*, 1–8. https://doi.org/10.1016/j.brainres.2016.02.050.

Budak, G., Srivastava, R., and Janga, S.C. (2017). Seten: a tool for systematic identification and comparison of processes, phenotypes, and diseases associated with RNA-binding proteins from condition-specific CLIP-seq profiles. Rna *23*, 836–846. https://doi.org/10.1261/rna.059089.116.

Cardinali, B., Di Cristina, M., and Pierandrei-Amaldi, P. (1993). Interaction of proteins with the mRNA for ribosomal protein L1 in*Xenopus*: structural characterization of*in vivo*complexes and identification of proteins that bind*in vivo*to its 5'UTR. Nucleic. Acids. Res. *21*, 2301–2308. https://doi.org/10.1093/nar/21.10.2301.

Chou, M.M., and Blenis, J. (1996). The 70 kDa S6 kinase complexes with and is activated by the Rho family G proteins Cdc42 and Rac1. Cell *85*, 573–583. https://doi.org/10.1016/s0092-8674(00)81257-x.

Corsini, N.S., Peer, A.M., Moeseneder, P., Roiuk, M., Burkard, T.R., Theussl, H.C., Moll, I., and Knoblich, J.A. (2018). Coordinated control of mRNA and rRNA processing controls embryonic stem cell pluripotency and differentiation. Cell Stem Cell *22*, 543–558.e12. https://doi.org/10.1016/j.stem.2018.03.002.

Cox, J., and Mann, M. (2008). MaxQuant enables high peptide identification rates, individualized p.p.b.-range mass accuracies and proteome-wide protein quantification. Nat. Biotechnol. *26*, 1367–1372. https://doi.org/10.1038/nbt.1511.

Dobin, A., Davis, C.A., Schlesinger, F., Drenkow, J., Zaleski, C., Jha, S., Batut, P., Chaisson, M., and Gingeras, T.R. (2013). STAR: ultrafast universal RNA-seq aligner. Bioinformatics *29*, 15–21. https://doi.org/10.1093/bioinformatics/bts635.

Edgar, R., Domrachev, M., and Lash, A.E. (2002). Gene Expression Omnibus: NCBI gene expression and hybridization array data repository. Nucleic. Acids. Res. *30*, 207–210. https://doi.org/10.1093/nar/30.1.207.

Eliseeva, I., Vorontsov, I., Babeyev, K., Buyanova, S., Sysoeva, M., Kondrashov, F., and Kulakovskiy, I. (2013). In silico motif analysis suggests an interplay of transcriptional and translational control in mTOR response. Translation (Austin) *1*, 18–24. https://doi.org/10.4161/trla.27469.

Farley, F.W., Soriano, P., Steffen, L.S., and Dymecki, S.M. (2000). Widespread recombinase expression using FLPeR (flipper) mice. Genesis *28*, 106–110. https://doi.org/10.1002/1526-968x(200011/12)28:3/4<106::aid-gene30>3.0.co;2-t.

Francois, J.C., Aid, S., Chaker, Z., Lacube, P., Xu, J., Fayad, R., Cote, F., Even, P., and Holzenberger, M. (2017). Disrupting IGF signaling in adult mice conditions leanness, resilient energy metabolism, and high growth hormone pulses. Endocrinology *158*, 2269–2283. https://doi.org/10.1210/en.2017-00261.

Gentleman, R.C., Carey, V.J., Bates, D.M., Bolstad, B., Dettling, M., Dudoit, S., Ellis, B., Gautier, L., Ge, Y., Gentry, J., et al. (2004). Bioconductor: open software development for computational biology and bioinformatics. Genome Biol. *5*, R80. https://doi.org/10.1186/gb-2004-5-10-r80.

Gerstberger, S., Hafner, M., and Tuschl, T. (2014). A census of human RNA-binding proteins. Nat. Rev. Genet. *15*, 829–845. https://doi.org/10.1038/nrg3813.

He, X., Arslan, A.D., Ho, T.T., Yuan, C., Stampfer, M.R., and Beck, W.T. (2014). Involvement of polypyrimidine tract-binding protein (PTBP1) in maintaining breast cancer cell growth and malignant properties. Oncogenesis *3*, e84. https://doi.org/10.1038/oncsis.2013.47.

He, X., Yuan, C., and Yang, J. (2015). Regulation and functional significance of CDC42 alternative splicing in ovarian cancer. Oncotarget *6*, 29651–29663. https://doi.org/10.18632/oncotarget.4865.

Heinz, S., Benner, C., Spann, N., Bertolino, E., Lin, Y.C., Laslo, P., Cheng, J.X., Murre, C., Singh, H., and Glass, C.K. (2010). Simple combinations of lineage-determining transcription factors prime cis-regulatory elements required for macrophage and B cell identities. Mol. Cell *38*, 576–589. https://doi.org/10.1016/j.molcel.2010.05.004.

Hentze, M.W., Castello, A., Schwarzl, T., and Preiss, T. (2018). A brave new world of RNA-binding proteins. Nat. Rev. Mol. Cell Biol *19*, 327–341. https://doi.org/10.1038/nrm.2017.130.

Hsieh, A.C., Liu, Y., Edlind, M.P., Ingolia, N.T., Janes, M.R., Sher, A., Shi, E.Y., Stumpf, C.R., Christensen, C., Bonham, M.J., et al. (2012). The translational landscape of mTOR signalling steers cancer initiation and metastasis. Nature *485*, 55–61. https://doi.org/10.1038/nature10912.

Inoue, D., Bradley, R.K., and Abdel-Wahab, O. (2016). Spliceosomal gene mutations in myelodysplasia: molecular links to clonal abnormalities of hematopoiesis. Genes. Dev. *30*, 989–1001. https://doi.org/10.1101/gad.278424.116.

Jaako, P., Flygare, J., Olsson, K., Quere, R., Ehinger, M., Henson, A., Ellis, S., Schambach, A., Baum, C., Richter, J., et al. (2011). Mice with ribosomal protein S19 deficiency develop bone marrow failure and symptoms like patients with Diamond-Blackfan anemia. Blood *118*, 6087–6096. https://doi.org/10.1182/blood-2011-08-371963.

Jefferies, H.B., Reinhard, C., Kozma, S.C., and Thomas, G. (1994). Rapamycin selectively represses translation of the "polypyrimidine tract" mRNA family. Proc. Natl. Acad. Sci. U S A. *91*, 4441–4445. https://doi.org/10.1073/pnas.91.10.4441.

Kang, R., Wan, J., Arstikaitis, P., Takahashi, H., Huang, K., Bailey, A.O., Thompson, J.X., Roth, A.F., Drisdel, R.C., Mastro, R., et al. (2008). Neural palmitoyl-proteomics reveals dynamic synaptic palmitoylation. Nature *456*, 904–909. https://doi.org/10.1038/nature07605.

Khajuria, R.K., Munschauer, M., Ulirsch, J.C., Fiorini, C., Ludwig, L.S., McFarland, S.K., Abdulhay, N.J., Specht, H., Keshishian, H., Mani, D.R., et al. (2018). Ribosome levels selectively regulate translation and lineage commitment in human hematopoiesis. Cell *173*, 90–103.e19. https://doi.org/10.1016/j.cell.2018.02.036.

Kos-Braun, I.C., Jung, I., and Kos, M. (2017). Tor1 and CK2 kinases control a switch between alternative ribosome biogenesis pathways in a growth-dependent manner. PLoS Biol. *15*, e2000245. https://doi.org/10.1371/journal.pbio.2000245.

Kuhn, R., Schwenk, F., Aguet, M., and Rajewsky, K. (1995). Inducible gene targeting in mice. Science *269*, 1427–1429. https://doi.org/10.1126/science.7660125.

Liberzon, A., Subramanian, A., Pinchback, R., Thorvaldsdottir, H., Tamayo, P., and Mesirov, J.P. (2011). Molecular signatures database (MSigDB) 3.0. Bioinformatics *27*, 1739–1740. https://doi.org/10.1093/bioinformatics/btr260.

Licatalosi, D.D., Mele, A., Fak, J.J., Ule, J., Kayikci, M., Chi, S.W., Clark, T.A., Schweitzer, A.C., Blume, J.E., Wang, X., et al. (2008). HITS-CLIP yields genome-wide insights into brain alternative RNA processing. Nature *456*, 464–469. https://doi.org/10.1038/nature07488.

Liu, J., Li, Y., Tong, J., Gao, J., Guo, Q., Zhang, L., Wang, B., Zhao, H., Wang, H., Jiang, E., et al. (2018). Long non-coding RNA-dependent mechanism to regulate heme biosynthesis and erythrocyte development. Nat. Commun. *9*, 4386. https://doi.org/10.1038/s41467-018-06883-x.

Liu, J., Zhang, J., Ginzburg, Y., Li, H., Xue, F., De Franceschi, L., Chasis, J.A., Mohandas, N., and An, X. (2013). Quantitative analysis of murine terminal erythroid differentiation in vivo: novel method to study normal and disordered erythropoiesis. Blood *121*, e43–e49. https://doi.org/10.1182/blood-2012-09-456079.

Love, M.I., Huber, W., and Anders, S. (2014). Moderated estimation of fold change and dispersion for RNA-seq data with DESeq2. Genome Biol. *15*, 550. https://doi.org/10.1186/s13059-014-0550-8.

Makeyev, E.V., Zhang, J., Carrasco, M.A., and Maniatis, T. (2007). The MicroRNA miR-124 promotes neuronal differentiation by triggering brain-specific alternative pre-mRNA splicing. Mol. Cell *27*, 435–448. https://doi.org/10.1016/j.molcel.2007.07.015.

Meyuhas, O., and Kahan, T. (2015). The race to decipher the top secrets of TOP mRNAs. Biochim. Biophys. Acta *1849*, 801–811. https://doi.org/10.1016/j.bbagrm.2014.08.015.

Mills, E.W., and Green, R. (2017). Ribosomopathies: There's strength in numbers. Science *358*, eaan2755. https://doi.org/10.1126/science.aan2755.

Mitchell, S.A., Spriggs, K.A., Bushell, M., Evans, J.R., Stoneley, M., Le Quesne, J.P., Spriggs, R.V., and Willis, A.E. (2005). Identification of a motif that mediates polypyrimidine tract-binding protein-dependent internal ribosome entry. Genes. Dev. *19*, 1556–1571. https://doi.org/10.1101/gad.339105.

Monzon-Casanova, E., Screen, M., Diaz-Munoz, M.D., Coulson, R.M.R., Bell, S.E., Lamers, G., Solimena, M., Smith, C.W.J., and Turner, M. (2018). The RNA-binding protein PTBP1 is necessary for B cell selection in germinal centers. Nat. Immunol. *19*, 267–278. https://doi.org/10.1038/s41590-017-0035-5.

Nandagopal, N., and Roux, P.P. (2015). Regulation of global and specific mRNA translation by the mTOR signaling pathway. Translation *3*, e983402. https://doi.org/10.4161/21690731.2014.983402.

Orkin, S.H., and Zon, L.I. (2008). Hematopoiesis: an evolving paradigm for stem cell biology. Cell *132*, 631–644. https://doi.org/10.1016/j.cell.2008.01.025.

Palangat, M., Anastasakis, D.G., Fei, D.L., Lindblad, K.E., Bradley, R., Hourigan, C.S., Hafner, M., and Larson, D.R. (2019). The splicing factor U2AF1 contributes to cancer progression through a noncanonical role in translation regulation. Genes. Dev. *33*, 482–497. https://doi.org/10.1101/gad.319590.118.

Park, D., Spencer, J.A., Koh, B.I., Kobayashi, T., Fujisaki, J., Clemens, T.L., Lin, C.P., Kronenberg, H.M., and Scadden, D.T. (2012). Endogenous bone marrow MSCs are dynamic, fate-restricted participants in bone maintenance and regeneration. Cell. Stem. Cell. *10*, 259–272. https://doi.org/10.1016/j.stem.2012.02.003.

Patro, R., Duggal, G., Love, M.I., Irizarry, R.A., and Kingsford, C. (2017). Salmon provides fast and bias-aware quantification of transcript expression. Nat. Methods. *14*, 417–419. https://doi.org/10.1038/nmeth.4197.

Paulson, R.F., Ruan, B., Hao, S., and Chen, Y. (2020). Stress erythropoiesis is a key inflammatory response. Cells *9*, 634. https://doi.org/10.3390/cells9030634.

Perez-Riverol, Y., Csordas, A., Bai, J., Bernal-Llinares, M., Hewapathirana, S., Kundu, D.J., Inuganti, A., Griss, J., Mayer, G., Eisenacher, M., et al. (2019). The PRIDE database and related tools and resources in 2019: improving support for quantification data. Nucleic. Acids. Res. *47*, D442–D450. https://doi.org/10.1093/nar/gky1106.

Pichon, X., A Wilson, L., Wilson, L.A., Stoneley, M., Bastide, A., King, H.A., Somers, J., E Willis, A., and Willis, A.E. (2012). RNA binding protein/RNA element interactions and the control of translation. Curr. Protein. Pept. Sci. *13*, 294–304. https://doi.org/10.2174/138920312801619475.

Pietras, E.M., Reynaud, D., Kang, Y.A., Carlin, D., Calero-Nieto, F.J., Leavitt, A.D., Stuart, J.M., Gottgens, B., and Passegue, E. (2015). Functionally distinct subsets of lineage-biased multipotent progenitors control blood production in normal and regenerative conditions. Cell. Stem. Cell. *17*, 35–46. https://doi.org/10.1016/j.stem.2015.05.003.

Pronk, C.J.H., and Bryder, D. (2011). Flow cytometry-based identification of immature myeloerythroid development. Methods. Mol. Biol. *699*, 275–293. https://doi.org/10.1007/978-1-61737-950-5_13.

Quinlan, A.R., and Hall, I.M. (2010). BEDTools: a flexible suite of utilities for comparing genomic features. Bioinformatics *26*, 841–842. https://doi.org/10.1093/bioinformatics/btq033.

Rappsilber, J., Mann, M., and Ishihama, Y. (2007). Protocol for micro-purification, enrichment, pre-fractionation and storage of peptides for proteomics using StageTips. Nat. Protoc. *2*, 1896–1906. https://doi.org/10.1038/nprot.2007.261.

Ray, D., Kazan, H., Cook, K.B., Weirauch, M.T., Najafabadi, H.S., Li, X., Gueroussov, S., Albu, M., Zheng, H., Yang, A., et al. (2013). A compendium of RNA-binding motifs for decoding gene regulation. Nature *499*, 172–177. https://doi.org/10.1038/nature12311.

Sawicka, K., Bushell, M., Spriggs, K.A., and Willis, A.E. (2008). Polypyrimidine-tract-binding protein: a multifunctional RNA-binding protein. Biochem. Soc. Trans. *36*, 641–647. https://doi.org/10.1042/bst0360641.

Schneider, R.K., Schenone, M., Ferreira, M.V., Kramann, R., Joyce, C.E., Hartigan, C., Beier, F., Brummendorf, T.H., Germing, U., Platzbecker, U., et al. (2016). Rps14 haploinsufficiency causes a block in erythroid differentiation mediated by S100A8 and S100A9. Nat. Med. *22*, 288–297. https://doi.org/10.1038/nm.4047.

Schoof, E.M., Lechman, E.R., and Dick, J.E. (2016). Global proteomics dataset of miR-126 overexpression in acute myeloid leukemia. Data. Brief. *9*, 57–61. https://doi.org/10.1016/j.dib.2016.07.035.

Severson, W.E., Mascolo, P.L., and White, M.W. (1995). Lymphocyte p56L32 is a RNA/DNA-binding protein which interacts with conserved elements of the murine L32 ribosomal protein mRNA. Eur. J. Biochem. *229*, 426–432. https://doi.org/10.1111/j.1432-1033.1995.0426k.x.

Signer, R.A.J., Magee, J.A., Salic, A., and Morrison, S.J. (2014). Haematopoietic stem cells require a highly regulated protein synthesis rate. Nature *509*, 49–54. https://doi.org/10.1038/nature13035.

Soneson, C., Love, M.I., and Robinson, M.D. (2015). Differential analyses for RNA-seq: transcript-level estimates improve gene-level inferences. F1000Res *4*, 1521. https://doi.org/10.12688/f1000research.7563.1.

Spellman, R., Llorian, M., and Smith, C.W. (2007). Crossregulation and functional redundancy between the splicing regulator PTB and its paralogs nPTB and ROD1. Mol. Cell. *27*, 420–434. https://doi.org/10.1016/j.molcel.2007.06.016.

Subramanian, A., Tamayo, P., Mootha, V.K., Mukherjee, S., Ebert, B.L., Gillette, M.A., Paulovich, A., Pomeroy, S.L., Golub, T.R., Lander, E.S., and Mesirov, J.P. (2005). Gene set enrichment analysis: a knowledge-based approach for interpreting genome-wide expression profiles. Proc. Natl. Acad. Sci. U S A. *102*, 15545–15550. https://doi.org/10.1073/pnas.0506580102.

Suckale, J., Wendling, O., Masjkur, J., Jager, M., Munster, C., Anastassiadis, K., Stewart, A.F., and Solimena, M. (2011). PTBP1 is required for embryonic development before gastrulation. PLoS One *6*, e16992. https://doi.org/10.1371/journal.pone.0016992.

Sun, Y.M., Wang, W.T., Zeng, Z.C., Chen, T.Q., Han, C., Pan, Q., Huang, W., Fang, K., Sun, L.Y., Zhou, Y.F., et al. (2019). CircMYBL2, a circRNA from MYBL2, regulates FLT3 translation by recruiting PTBP1 to promote FLT3-ITD AML progression. Blood *134*, 1533–1546. https://doi.org/10.1182/blood.2019000802.

Sun, Z., Zhu, M., Lv, P., Cheng, L., Wang, Q., Tian, P., Yan, Z., and Wen, B. (2018). The long noncoding RNA Lncenc1 maintains naive states of mouse ESCs by promoting the glycolysis pathway. Stem. Cell. Rep. *11*, 741–755. https://doi.org/10.1016/j.stemcr.2018.08.001.

Tahmasebi, S., Amiri, M., and Sonenberg, N. (2018). Translational control in stem cells. Front. Genet. *9*, 709. https://doi.org/10.3389/fgene.2018.00709.

Tcherkezian, J., Cargnello, M., Romeo, Y., Huttlin, E.L., Lavoie, G., Gygi, S.P., and Roux, P.P. (2014). Proteomic analysis of cap-dependent translation identifies LARP1 as a key regulator of 5'TOP mRNA translation. Genes Dev. *28*, 357–371. https://doi.org/10.1101/gad.231407.113.

Thoreen, C.C., Chantranupong, L., Keys, H.R., Wang, T., Gray, N.S., and Sabatini, D.M. (2012). A unifying model for mTORC1-mediated regulation of mRNA translation. Nature *485*, 109–113. https://doi.org/10.1038/nature11083.

Trapnell, C., Hendrickson, D.G., Sauvageau, M., Goff, L., Rinn, J.L., and Pachter, L. (2013). Differential analysis of gene regulation at transcript resolution with RNA-seq. Nat. Biotechnol. *31*, 46–53. https://doi.org/10.1038/nbt.2450.

Van Nostrand, E.L., Freese, P., Pratt, G.A., Wang, X., Wei, X., Xiao, R., Blue, S.M., Chen, J.Y., Cody, N.A.L., Dominguez, D., et al. (2020). A large-scale binding and functional map of human RNA-binding proteins. Nature *583*, 711–719. https://doi.org/10.1038/s41586-020-2077-3.

Vitting-Seerup, K., Porse, B.T., Sandelin, A., and Waage, J. (2014). SpliceR: an R package for classification of alternative splicing and prediction of coding

potential from RNA-seq data. BMC. Bioinformatics. *15*, 81. https://doi.org/10.1186/1471-2105-15-81.

Vitting-Seerup, K., and Sandelin, A. (2019). IsoformSwitchAnalyzeR: analysis of changes in genome-wide patterns of alternative splicing and its functional consequences. Bioinformatics *35*, 4469–4471. https://doi.org/10.1093/bioinformatics/btz247.

Vuong, J.K., Lin, C.H., Zhang, M., Chen, L., Black, D.L., and Zheng, S. (2016). PTBP1 and PTBP2 serve both specific and redundant functions in neuronal Pre-mRNA splicing. Cell. Rep. *17*, 2766–2775. https://doi.org/10.1016/j.celrep.2016.11.034.

Wang, M., Anikin, L., and Pestov, D.G. (2014). Two orthogonal cleavages separate subunit RNAs in mouse ribosome biogenesis. Nucleic. Acids. Res. *42*, 11180–11191. https://doi.org/10.1093/nar/gku787.

Wang, M., and Pestov, D.G. (2016). Quantitative northern blot analysis of mammalian rRNA processing. Methods Mol. Biol. *1455*, 147–157. https://doi.org/10.1007/978-1-4939-3792-9_12.

Wilson, N.K., Kent, D.G., Buettner, F., Shehata, M., Macaulay, I.C., Calero-Nieto, F.J., Sanchez Castillo, M., Oedekoven, C.A., Diamanti, E., Schulte, R., et al. (2015). Combined single-cell functional and gene expression analysis resolves heterogeneity within stem cell populations. Cell Stem Cell *16*, 712–724. https://doi.org/10.1016/j.stem.2015.04.004.

Wojtowicz, E.E., Lechman, E.R., Hermans, K.G., Schoof, E.M., Wienholds, E., Isserlin, R., van Veelen, P.A., Broekhuis, M.J., Janssen, G.M., Trotman-Grant, A., et al. (2016). Ectopic miR-125a expression induces long-term repopulating stem cell capacity in mouse and human hematopoietic progenitors. Cell Stem Cell *19*, 383–396. https://doi.org/10.1016/j.stem.2016.06.008.

Xu, J., Gontier, G., Chaker, Z., Lacube, P., Dupont, J., and Holzenberger, M. (2014). Longevity effect of IGF-1R(+/-) mutation depends on genetic background-specific receptor activation. Aging Cell *13*, 19–28. https://doi.org/10.1111/acel.12145.

Xue, Y., Ouyang, K., Huang, J., Zhou, Y., Ouyang, H., Li, H., Wang, G., Wu, Q., Wei, C., Bi, Y., et al. (2013). Direct conversion of fibroblasts to neurons by reprogramming PTB-regulated microRNA circuits. Cell *152*, 82–96. https://doi.org/10.1016/j.cell.2012.11.045.

Xue, Y., Zhou, Y., Wu, T., Zhu, T., Ji, X., Kwon, Y.S., Zhang, C., Yeo, G., Black, D.L., Sun, H., and Fu, X.D. (2009). Genome-wide analysis of PTB-RNA interactions reveals a strategy used by the general splicing repressor to modulate exon inclusion or skipping. Mol. Cell *36*, 996–1006. https://doi.org/10.1016/j.molcel.2009.12.003.

Yap, K., Mukhina, S., Zhang, G., Tan, J.S.C., Ong, H.S., and Makeyev, E.V. (2018). A short tandem repeat-enriched RNA assembles a nuclear compartment to control alternative splicing and promote cell survival. Mol. Cell *72*, 525–540.e13. https://doi.org/10.1016/j.molcel.2018.08.041.

Yap, K., Xiao, Y., Friedman, B.A., Je, H.S., and Makeyev, E.V. (2016). Polarizing the neuron through sustained co-expression of alternatively spliced isoforms. Cell Rep. *15*, 1316–1328. https://doi.org/10.1016/j.celrep.2016.04.012.

Zhang, X., Chen, M.H., Wu, X., Kodani, A., Fan, J., Doan, R., Ozawa, M., Ma, J., Yoshida, N., Reiter, J.F., et al. (2016). Cell-type-specific alternative splicing governs cell fate in the developing cerebral cortex. Cell *166*, 1147–1162.e15. https://doi.org/10.1016/j.cell.2016.07.025.

STAR★METHODS

KEY RESOURCES TABLE

REAGENT or RESOURCE	SOURCE	IDENTIFIER
Antibodies		
Anti-Human/Mouse CD45R (B220) APC (clone RA3- 6B2)	eBioscience/Thermo Fisher Scientific	Cat# 17-0452-82; RRID:AB_469395
Anti-Human/Mouse CD45R (B220) PE-Cy5 (clone RA3- 6B2)	eBioscience/Thermo Fisher Scientific	Cat# 15-0452-83; RRID:AB_468756
Anti-Mouse CD3e PE-Cy5 (clone 145-2C11)	eBioscience/Thermo Fisher Scientific	Cat# 15-0031-82; RRID:AB_468690
Anti-Mouse CD4 PE-Cy5 (clone GK1.5)	eBioscience/Thermo Fisher Scientific	Cat# 15-0041-81; RRID:AB_468694
Anti-Mouse CD8a PE-Cy5 (clone 53-6.7)	eBioscience/Thermo Fisher Scientific	Cat# 15-0081-81; RRID:AB_468705
Anti-Mouse CD16/CD32 (Mouse BD Fc Block) Purified	BD Biosciences	Cat# 553142; RRID:AB_394657
Anti-Mouse CD16/CD32 Alexa Fluor 700 (clone 93)	eBioscience/Thermo Fisher Scientific	Cat# 56-0161-82; RRID: AB_493994
Anti-Mouse CD135 (Flt3) PE (Clone A2F10)	eBioscience/Thermo Fisher Scientific	Cat# 12-1351-83; RRID:AB_465860
Anti-Mouse CD117 (c-Kit) APC-eFluor 780 (clone 2B8)	eBioscience/Thermo Fisher Scientific	Cat# 47-1171-82; RRID:AB_1272177
Anti-Mouse Ly-6G (Gr-1) PE-Cy5 (clone RB6-8C5)	eBioscience/Thermo Fisher Scientific	Cat# 15-5931-82; RRID:AB_468813
Anti-Mouse CD127 Biotin (clone A7R34)	eBioscience/Thermo Fisher Scientific	Cat# 13-1271-82; RRID:AB_466588
Anti-Mouse/human CD11b APC (clone M1/70)	eBioscience/Thermo Fisher Scientific	Cat# 17-0112-82; RRID:AB_469343
Anti-mouse/human CD11b PE-Cy5 (clone M1/70)	BioLegend	Cat# 101210; RRID:AB_312793
Anti-Mouse TER-119 PE-Cy5 (clone Ter119)	eBioscience/Thermo Fisher Scientific	Cat# 15-5921-81; RRID:AB_468809
Anti-Human/Mouse CD45R (B220) Alexa Fluor 700 (clone RA3- 6B2)	eBioscience/Thermo Fisher Scientific	Cat# 56-0452-82; RRID:AB_891458
Anti-mouse CD41 FITC (clone MWReg30)	eBioscience/Thermo Fisher Scientific	Cat# 11-0411-82; RRID: AB_763481
Anti-mouse CD41 eFluor450 (clone MWReg30)	eBioscience	Cat# 48-0411-82; RRID: AB_1582238
Anti-mouse CD105 PE (clone Mj7/18)	eBioscience	Cat# 12-1051-82; RRID: AB_657524
Anti-mouse Ly-6A/E (Sca-1) APC (clone D7)	eBioscience	Cat# 17-5981-82; RRID: AB_469487
Anti-mouse Flt3 PECF594 (Clone A2F10)	BD Biosciences	Cat# 562537; RRID: AB_2737639
Anti-mouse CD150 BV650 (clone TC15-12F12.2)	Biolegend	Cat# 115931; RRID: AB_2562402
Anti-mouse CD48 PeCy7 (clone HM48-1)	Biolegend	Cat# 103423; RRID: AB_2075050
Anti-mouse CD44 FITC (clone IM7)	eBioscience	Cat# 11-0441-82; RRID: AB_465045
Anti-mouse Ter119 PeCy7 (clone Ter119)	eBioscience	Cat# 25-5921-82; RRID: AB_469661
Anti-mouse CD71 FITC (clone C2)	BD Biosciences	Cat# 561936; RRID: AB_11153845
Anti-mouse Ly-6G (Gr-1) PE (clone RB6-8C5)	eBioscience	Cat#12-5931-82; RRID: AB_466045
Anti-mouse CD45.1 FITC (clone A20)	eBioscience/Thermo Fisher Scientific	Cat# 11-0453-82; RRID: AB_465058
Anti-mouse CD45.2 PE ((clone 104)	BD Biosciences	Cat# 560695; RRID: AB_1727493
anti-Ki67-FITC (clone B56)	BD Biosciences	Cat# 556026; RRID: AB_396302
anti-BrdU-FITC (clone 3D4)	BD Biosciences	Cat# 556028; RRID: AB_396304
Chemicals, peptides, and recombinant proteins		
5-Ethynyl-uridine	Jena Bioscience	Cat#CLK-N002-10
O-propargyl-puromycin	Medchem Source	Custom synthesized

(*Continued on next page*)

Continued

REAGENT or RESOURCE	SOURCE	IDENTIFIER
Phenylhydrazine	Sigma Aldrich	Cat#P26252
DAPI	Invitrogen	Cat#D3571
2′,7′-dichlorofluorescein diacetate	Invitrogen	Cat#D399
CFSE	Invitrogen	Cat#C34570
Erythropoietin	Stem Cell Technologies	Cat#78007
Recombinant murine Stem Cell Factor	Peprotech	Cat# 250-03
Holotransferrin	Sigma	Cat# T0665
Recombinant human Insulin	Sigma	Cat# I9278
Critical commercial assays		
Click-iT Plus OPP Alexa Fluor 488 Protein Synthesis Assay Kit	Thermo Fisher	Cat# C10456
Click-iT Plus Alexa Fluor 488 Picolyl Azide Toolkit	Thermo Fisher	Cat# C10641
Methocult M3434	Stem Cell Technologies	Cat#03434
Methocult M3436	Stem Cell Technologies	Cat#03436
Ovation RNA-seq System V2	NuGEN	Cat# 7102-32
Ovation Ultralow System V2	NuGEN	Cat#0344-32
RNeasy micro kit	QIAGEN	Cat#74004
FITC BrdU flow kit	BD Biosciences	Cat# 559619; RRID:AB_2617060
Deposited data		
RNA-seq	This paper	GEO: GSE165682
Mass spectrometry	This paper	Proteome exchange: PXD023879
eCLIP	Van Nostrand et al. (2020)	Encode: ENCSR981WKN
eCLIP	Van Nostrand et al. (2020)	Encode: ENCSR657TZB
eCLIP	Van Nostrand et al. (2020)	Encode: ENCSR862QCH
Seten	Budak et al. (2017)	http://www.iupui.edu/~sysbio/seten/
iCLIP-seq	Vuong et al. (2016)	GEO: GSM2259090
iCLIP-seq	Vuong et al. (2016)	GEO: GSM2259093
human 45s pre-ribosomal DNA sequence RNA45SN5	NCBI/Nucleotide	NCBI: NR_046235.3
Mouse reference genome mm10/GRCm38	Genome Reference Consortium	N/A
Mouse reference genome mm9/NCBI37	Genome Reference Consortium	N/A
Experimental models: Organisms/strains		
Mouse: $Ptbp1^{fl/fl}$: B6J.129-$Ptbp1^{tm1Msol}$	Suckale et al. (2011)	Michele Solimena
Mouse: Mx1Cre; Tg(Mx1-cre)1Cgn	Kuhn et al. (1995)	N/A
Mouse: *Igf1r*$^{+/-}$	Xu et al. (2014)	Martin Holzenberger
Mouse: C57BL/6JBomTac	Taconic	N/A
Mouse: B6.SJL-*Ptprc*^{a}/BoyAiTac	Taconic	N/A
Oligonucleotides		
Primer for *Ptbp1* genotyping PCR: CCTCATTTGCTGTCCTGGTT	This paper	N/A
Primer for *Ptbp1* genotyping PCR: CCCTGGTGTCCTGTCATCTT	This paper	N/A
Primer for *Ptbp1* genotyping PCR: GGGCAGGACTGCTGAGTG	This paper	N/A
Oligonucleotide probes used for Northern blot analysis. See Table S6.	Wang and Pestov (2016)	N/A
Recombinant DNA		
GFP-cdc42palm	Kang et al. (2008)	Addgene plasmid#20141
GFP-cdc42prenyl	Kang et al. (2008)	Addgene plasmid#20142

(*Continued on next page*)

Continued

REAGENT or RESOURCE	SOURCE	IDENTIFIER
MIGR1-Cdc42-1	This paper	N/A
MIGR1-Cdc42-2	This paper	N/A
Software and algorithms		
FlowJo	BD	https://www.flowjo.com/solutions/flowjo; RRID:SCR_008520
Prism	GraphPad	https://www.graphpad.com/; RRID:SCR_002798
bcbio-nextgen	N/A	https://github.com/bcbio/bcbio-nextgen
STAR aligner	Dobin et al., 2013	https://github.com/alexdobin/STAR
Salmon	Patro et al., 2017	https://combine-lab.github.io/salmon/
FastQC	Babraham Bioinformatics	https://www.bioinformatics.babraham.ac.uk/projects/fastqc/
R/Bioconductor	Gentleman et al., 2004	https://www.R-project.org/
GSEA	Subramanian et al., 2005	http://software.broadinstitute.org/gsea/index.jsp
tximport v1.10.1	Soneson et al. (2015)	https://bioconductor.org/packages/3.8/bioc/html/tximport.html
DESeq2 v1.22.2	Love et al., 2014	https://bioconductor.org/packages/release/bioc/html/DESeq2.html
Bedtools	Quinlan and Hall (2010)	http://bedtools.readthedocs.io/en/latest/
DEXSeq	Anders et al. (2012)	https://bioconductor.org/packages/release/bioc/html/DEXSeq.html
Cuffdiff	Trapnell et al. (2013)	http://cole-trapnell-lab.github.io/cufflinks/
IsoformSwitchAnalyzeR v1.9.3	Vitting-Seerup and Sandelin (2019)	https://bioconductor.org/packages/release/bioc/html/IsoformSwitchAnalyzeR.html
seqLogo	N/A	https://bioconductor.org/packages/release/bioc/html/seqLogo.html
HOMER	Heinz et al., 2010	http://homer.ucsd.edu/homer/
MaxQuant v 1.5.2.8	Cox and Mann (2008)	https://www.maxquant.org/
PINT	Wojtowicz et al. (2016)	N/A
Other		
MSigDB v7.2 gene sets	Liberzon et al. (2011)	http://software.broadinstitute.org/gsea/msigdb

RESOURCE AVAILABILITY

Lead contact

Further information and requests for resources and reagents should be directed to and will be fulfilled by the lead contact, Bo T. Porse (bo.porse@finsenlab.dk).

Materials availability

Plasmids generated in this study have been deposited to Addgene; Cat #179517 and #179518.

Data and code availability

- RNA-seq data have been deposited at GEO and are publicly available as of the date of publication. Accession numbers are listed in the key resources table.
- Proteomics data have been deposited at Proteome Exchange and are publicly available as of the date of publication. Accession numbers are listed in the key resources table.
- This paper analyzes existing, publicly available data. The accession numbers for these datasets are listed in the key resources table.
- This paper does not report original code.
- Any additional information required to reanalyze the data reported in this paper is available from the lead contact upon request.

EXPERIMENTAL MODEL AND SUBJECT DETAILS

Mice were bred and housed in individually ventilated cages (eight mice/cage) at the Department of Experimental Medicine at the University of Copenhagen according to institutional guidelines. Experiments were carried out with permissions from the Danish Animal Research Ethical Committee. 10–14 wk old female mice were used for all analyses unless specifically stated. All mice used in this study have been back-crossed at least six generations to a C57BL/6 background.

To generate the *Ptbp1*$^{fl/fl}$ conditional allele, we made use of the multi-purpose *Ptbp1* allele described previously (Suckale et al., 2011). Briefly, the frt-flanked stop/detection cassette was removed by intercrossing with ROSA26:FLPe knock in mice (129S4/SvJaeSor-*Gt(ROSA)26Sor*$^{tm1(FLP1)Dym}$/J) (Farley et al., 2000), thereby generating a conditional allele where exon 3–7 of *Ptbp1* is flanked by LoxP sites (*Ptbp1*$^{fl/fl}$). *Ptbp1*$^{fl/fl}$ mice were intercrossed with Mx1Cre transgenic mice (Tg(Mx1-cre)1Cgn) (Kuhn et al., 1995), and conditional deletion was obtained by 2–3 intraperitoneal injections of 200 μl polyinosinic-polycytidylic acid (poly-IC) (1.5 mg/mL, GE-Healthcare), generating a *Ptbp1* null allele (*Ptbp1*^{KO}). *Ptbp1*$^{fl/fl}$ littermates of the same sex from respective breedings were treated with poly-IC and assigned to experimental groups as controls. All analyses were performed three wk after poly-IC injection of 10–14-wk-old female mice, unless specifically stated. Heterozygous *Igf1r* knockout mice (*Igf1r*$^{+/-}$) (Xu et al., 2014) were generated by CreERT2-mediated inactivation of the conditional *Igf1r* allele (Francois et al., 2017) and subsequent segregation breeding on a C57BL/6 genetic background. Wildtype littermates served as controls. Colonies of C57BL/6 (C57BL/6JBomTac) and B6.SJL (B6.SJL-*Ptprc*^{a}/BoyAiTac) wildtype mice from Taconic were kept at the Department of Experimental Medicine at the University of Copenhagen, with colony-renewal every fifth generation through embryo-derivation.

METHOD DETAILS

Genotyping

A three-primer system (CCTCATTTGCTGTCCTGGTT; CCCTGGTGTCCTGTCATCTT; GGGCAGGACTGCTGAGTG) was used for PCR genotyping and recombination of the *Ptbp1* locus, resulting in bands of the following sizes: 287 bp (*Ptbp1*$^{fl/fl}$), 249 bp (*Ptbp1*^{KO}) and 208 bp (*Ptbp1*$^{+/+}$) (Figure S1A).

Transplantations

10–14 wk old congenic (B6.SJ/L (CD45.1^{+})) female recipients were lethally irradiated (900 cGy) 24 hours prior to transplantation through tail vein injection. Irradiated mice were supplemented with ciproflaxin in the drinking water (100 mg/L; Actavis or Sigma) for two wk. Blood samples were drawn to monitor engraftment at 3, 8, and 16 wk post transplantation and BM was analyzed at 16–18 wk post transplantation. For the competitive repopulation assay, 300 FACS sorted HSCs (LSK, CD150^{+}, CD48^{-}, CD45.2^{+}) from *Ptbp1*$^{fl/fl}$ or *Ptbp1*^{KO} mice were transplanted together with 400,000 congenic BM support cells (CD45.1^{+}) into 10–14 wk old congenic (CD45.1^{+}) female recipients through tail vein injection. For serial transplantations, 5x10^{6} BM cells were transplanted into primary recipients. Primary recipient mice were sacrificed after 16 wk, after which 5x10^{6} BM cells were transplanted into secondary recipients, and similarly after another 16 wk, to tertiary recipients. Alternatively, 300 FACS sorted HSCs (LSK, CD150^{+}, CD48^{-}, CD45.2^{+}) from the primary recipients were isolated and transplanted in a competitive repopulation experiment. For reverse transplantations, *Ptbp1*$^{fl/fl}$ or *Ptbp1*^{KO} mice were used as recipients five months after poly-IC injection. *Ptbp1*$^{fl/fl}$ or *Ptbp1*^{KO} mice were irradiated (900 cGy) 24 hours prior to injection of 5x10^{6} congenic wildtype BM cells (CD45.1^{+}).

Homing assays

CFSE-based homing

c-kit^{+} cells from *Ptbp1*$^{fl/fl}$ or *Ptbp1*^{KO} mice were incubated with 10 μM CFSE (Invitrogen) for 10 min at 37 C° and washed twice. Wildtype recipients were lethally irradiated 24 hours prior to injection of CFSE labeled cells at a dose of 2.5x10^{6} CFSE labeled c-kit^{+} cells per recipient. Injected mice were sacrificed three hours later and CFSE^{+} cells in BM and spleen were analyzed by flow cytometry.

Competitive repopulation-based homing

25x10^{6} BM cells from *Ptbp1*$^{fl/fl}$ or *Ptbp1*^{KO} mice (CD45.2) were transplanted to lethally irradiated congenic (CD45.1) recipients. Recipients were sacrificed after three hours, and the equivalent of 1/6 femur was immediately re-transplanted into another set of lethally irradiated recipients (CD45.1) together with 5x10^{5} BM competitor cells (CD45.1) and long-term engraftment was monitored as described above.

Phenylhydrazine treatment

For RBC recovery challenge, mice were injected with phenylhydrazine (Sigma-Aldrich) at 50 mg/kg on two consecutive days.

Colony assays

BM cells, splenocytes or PB were seeded in M3434 or M3436 semisolid methylcellulose medium (Stem Cell Technologies) according to manufacturer's protocol and colonies were scored by light microscopy.

Peripheral blood analysis by hematocytometry

PB samples were collected in EDTA-coated tubes and analyzed on a Sysmex-KX1 automated hematocytometer.

Histology

Femurs were dissected and kept in 4% PFA at 4°C for a minimum of 24 hours, after which they were stored in 70% ethanol. The bones were decalcified in a 10% water solution of EDTA, adjusted to pH 7.4, for two hours and 20 min at 50°C. To ensure complete decalcification, the femurs were stored in fresh 10% EDTA, pH 7.4, for three days at 4°C. They were then rinsed under running ionized water for one hour, dehydrated with 70%, 96% and 99% ethanol, followed by xylene, and subsequently embedded in paraffin. The embedded femurs were sectioned at 2.5 μm on a Leica SM2000R microtome and stained with Hematoxylin/Eosin after rehydration. Images were scanned by NanoZoomer-XR digital slide scanner and images captured by NDP.view 2 at 10x resolution.

Flow cytometry

BM (tibia, femur and iliac bones) and spleen were harvested and single-cell suspensions were obtained in PBS/3% fetal calf serum (FCS). For sorting of HSPC populations, BM cells were c-kit-enriched prior to antibody staining by CD117 magnetic microbeads followed by magnetic separation on LS-columns (Miltenyi Biotec) according to manufacturer's protocol. Where appropriate, Fc-receptor blocking was performed prior to antibody staining using purified FcgRII/III (clone 93, BD Pharmingen). PB samples were obtained in EDTA-coated tubes and RBC lysis was performed by incubation in Pharmlyse (BD Pharmingen). Samples were analyzed or FACS sorted on BD LsrII, BD FACS Canto, BD Aria I or BD Aria III.

Antibodies used for HSPC analysis

CD41 (clone MWReg30); CD105 (clone Mj7/18); Sca-1 (clone D7); FcgRII/III (clone 93); c-Kit (clone 2B8); Flt3 (clone A2F10); CD127 (clone A7R34), all eBioscience or BD Pharmingen. CD150 (clone TCF15-12F12.2, Biolegend), CD48 (clone HM48-1, Biolegend). For additional delineation of late erythrocytes, CD44 (clone IM7) was used as noted in figures.

Antibodies used for analysis or exclusion of mature lineages in blood and BM

Ter119 (clone Ter119); CD71 (clone C2); Gr1 (clone RB6-8C5); B220 (clone RA3-6B2) and CD3e (clone 145-2C11, all from eBioscience or BD Pharmingen), Mac1 (clone M1/70, from eBioscience or Biolegend); CD4 (clone GK1.5, eBioscience) and CD8a (clone 53-6.7, eBioscience). Separation of donor/recipient cells was performed using CD45.1 (clone A20) and CD45.2 (clone 104), both from eBioscience. Viability was detected by adding 7AAD or DAPI (both from Invitrogen) to the cell suspensions immediately prior to analysis/sort.

Cell cycle analysis

BM was isolated and samples adjusted to equal cell numbers. Cells were incubated with antibodies against cell-surface markers, fixed in 4% PFA for 10 min at RT followed by permeabilization with 0.1% saponin in PBS + 3% FCS for 45 min at RT. Next, cells were stained with anti-Ki67-FITC (clone B56) and 0.5 μg/mL DAPI (Invitrogen) and analyzed by flow cytometry.

Measurement of intracellular ROS

To measure the generation of ROS in HSCs, BM was harvested, c-kit enriched and stained for cell-surface markers. Cells were then incubated with 2′,7′-dichlorofluorescein diacetate (DCFDA, 1.25μM, Invitrogen) for 30 min at 37°C and analyzed by flow cytometry.

BrdU in vivo *proliferation analysis*

5-Bromo-2′-deoxyuridine (BrdU) (2 mg/mouse) was intraperitoneally injected three hours before sacrifice. BM cells were incubated with antibodies against cell-surface markers, fixed in 4% PFA for 10 min at RT followed by permeabilization with 0.1% saponin in PBS + 3% FCS for 45 min at RT. Next, cells were stained with anti-BrdU-FITC (clone 3D4) and analyzed by flow cytometry.

In vivo *protein synthesis assay*

To measure protein synthesis *in vivo*, O-propargyl-puromycin (50 mg/kg, Medchem Source) was intraperitoneally injected one hour before sacrifice, and BM was analyzed as previously described (Signer et al., 2014). Briefly, BM cells were stained with appropriate cell-surface markers, then fixed in 1% PFA for 15 min on ice followed by permeabilization in PBS/FCS 0.1% Saponin for 5 min at RT. The copper-catalyzed azide-alkyne cycloaddition was performed using the Click-iT Plus OPP Alexa Fluor 488 Protein Synthesis Assay Kit or the Click-iT Plus Alexa Fluor 488 Picolyl Azide Toolkit (ThermoFisher).

RNA synthesis measurement in vitro

To measure the rate of *in vitro* RNA synthesis, $3x10^6$ c-kit$^+$ cells were seeded in 1 mL IMDM, 10% FCS, 100 ng/mL mSCF (Peprotech) and 1 mM 5-Ethynyl-uridine (5-EU) (Jena Bioscience#CLK-N002-10) and incubated for one hour at 37°C. Following incubation, cells were harvested and stained with antibodies to identify myeloid-erythroid progenitors, then fixed in 1% PFA, 15 min on ice, followed by permeabilization in PBS/FCS 0.1% Saponin for 5 min at RT. 5-EU incorporation was detected using the Click-iT Plus Alexa Fluor 488 Picolyl Azide Toolkit (ThermoFisher).

Terminal erythroid differentiation *in vitro* assay

Erythroid *in vitro* differentiation was performed according to (Schneider et al., 2016). CFU-Es (Lin$^-$ Sca-1$^-$ c-kit$^+$ CD41$^-$ FcgRII/III$^-$ CD150$^-$ CD105$^+$) were FACS sorted and seeded in fibronectin-coated (2 μg/cm2) tissue-culture wells. Induction of erythroid

differentiation was performed in IMDM supplemented with 10 units/ml Epo (Stem Cell Technologies), 10 ng/ml SCF (Peprotech), 10μM dexamethasone (Sigma), 15% FCS, 1% detoxified BSA, 200 μg/ml holotransferrin (Sigma), 10 μg/ml recombinant human insulin (Sigma), 2 mM L-glutamine, 10^{-4} M β-mercaptoethanol and penicillin/streptomycin. The medium was replaced after 48 hours by maintenance medium consisting of IMDM with 20% FCS, 2 mM L-glutamine and 10^{-4} M β-mercaptoethanol. After 6 days of culture, erythroid cells were analysed by FACS for expression of Ter119 and CD71, with exclusion of dead cells by 7AAD.

In vivo protein synthesis analysis in BM chimeras

Cdc42-1 and *Cdc42*-2 retroviral expression constructs were generated by BglI/EcoRI sub-cloning of the respective isoform cDNA cassettes from plasmids generated by Kang et al. (Kang et al., 2008), into the MIGR1 retroviral expression vector. Viral supernatant was generated by transfection of Phoenix-Eco cells. BM cells from wildtype B6.SJ/L mice were c-kit-enriched by CD117 magnetic bead enrichment (Miltenyi) and pre-stimulated in RPMI with 15% FCS, 50 ng/mL murine SCF (PeproTech), 50 ng/mL human IL-6 (PeproTech) and 10 ng/mL murine IL-3 (Peprotech) for two days. Pre-stimulated cells were transduced on two consecutive days by spin-oculation of viral supernatant on Retronectin-coated wells (Takara) and then transplanted into lethally irradiated C57BL/6 recipients. After four wk of engraftment, BM was analyzed for *in vivo* protein synthesis together with CD45.1 and Ter119 expression. $5x10^6$ BM cells from *Igf1r*$^{+/-}$ or wildtype littermate controls (CD45.2$^+$; two donors per genotype) were transplanted into 10–14 wk old congenic (CD45.1$^+$) female recipients through tail vein injection. After four wk of engraftment, BM was analyzed for *in vivo* protein synthesis together with CD45.1/2 and Ter119 expression.

RNA-seq

HSCs (LSK, CD150$^+$ CD48$^-$), preMegEs (Lin$^-$ Sca-1$^-$ c-kit$^+$ CD41$^-$ FcgRII/III $^-$ CD150$^+$ CD105$^-$) and preCFU-Es (Lin$^-$ Sca-1$^-$ c-kit$^+$ CD41$^-$ FcgRII/III $^-$ CD150$^+$ CD105$^+$) were FACS sorted and total RNA was isolated using the RNeasy micro kit (Qiagen). RNA was subjected to double-stranded cDNA synthesis by help of the Ovation RNA-Seq System V2 (NuGEN). Sequencing libraries were prepared using the Ovation Ultralow System V2 (NuGEN). The indexed cDNA libraries were multiplexed and subjected to 100 cycles paired-end sequencing on the HiSeq2000 system (Illumina) at the Danish National High Throughput DNA Sequencing Centre.

Global proteomics analysis

For the global proteomics analysis, 80,000–100,000 preMegEs (Lin$^-$ Sca-1$^-$ c-kit$^+$ CD41$^-$ FcgRII/III $^-$ CD150$^+$ CD105$^-$) and preCFU-Es (Lin$^-$ Sca-1$^-$ c-kit$^+$ CD41$^-$ FcgRII/III $^-$ CD150$^+$ CD105$^+$) were flow sorted and washed twice with ice-cold PBS. For the CDC42 isoform over-expression samples, 100,000 GFP$^+$ cells were flow sorted and washed twice with ice-cold PBS. Resulting samples were subjected to sample preparation as described previously (Schoof et al., 2016). Cells were lysed using 20 μL of lysis buffer (consisting of 6 M guanidinium hydrochloride, 10 mM TCEP, 40 mM CAA and 100 mM Tris pH8.5). Samples were boiled at 95°C for 5 minutes, after which they were sonicated on high for 3 × 10 seconds in a Bioruptor sonication water bath (Diagenode) at 4°C. Samples were diluted 1:3 with 10% acetonitrile, 25 mM Tris pH 8.5, LysC (MS grade, Wako) was added in a 1:50 (enzyme to protein) ratio, and samples were incubated at 37°C for four hours. Samples were further diluted to 1:10 with 10% acetonitrile, 25 mM Tris pH 8.5, trypsin (MS grade, Promega) was added in a 1:100 (enzyme to protein) ratio, and samples were incubated overnight at 37°C. Enzyme activity was quenched by adding 2% trifluoroacetic acid (TFA) to a final concentration of 1%. Prior to mass spectrometry analysis, the peptides were desalted and fractionated on in-house packed SCX Stagetips (Rappsilber et al., 2007). For each sample, three discs of SCX material (3M Empore) were packed in a 200 μL tip, and the SCX material activated with 80 μL of 100% acetonitrile (HPLC grade, Sigma). The tips were equilibrated with 80 μL of 0.2% TFA, after which the samples were loaded using centrifugation at 4,000 rpm. After washing the tips twice with 100 μL of 0.2% TFA, two initial fractions were eluted into clean 500 μL Eppendorf tubes using 75 and 300 mM ammonium acetate in 20% acetonitrile, 0.5% formic acid respectively. The final fraction was eluted using 5% ammonium hydroxide, 80% acetonitrile. The eluted peptides were frozen on dry ice and concentrated in an Eppendorf speedvac, and re-constituted in 1% TFA, 2% acetonitrile for Mass Spectrometry (MS) analysis.

Mass spectrometry acquisition

For the preMegE and preCFU samples, peptides were loaded onto a 2cm C18 trap column (ThermoFisher 164705), connected in-line to a 50cm C18 reverse-phase analytical column (Thermo EasySpray ES803) using 100% Buffer A (0.1% Formic acid in water) at 750bar, using the Thermo EasyLC 1000 HPLC system in a single-column setup and the column oven operating at 45°C. Peptides were eluted over a 200 min gradient ranging from 5 to 48% of 100% acetonitrile, 0.1% formic acid at 250 nL/min, and the Orbitrap Fusion (Thermo Fisher Scientific) was run in a three second MS-OT, ddMS2-IT-HCD top speed method. Full MS spectra were collected at a resolution of 120,000, with an AGC target of 4×10^5 or maximum injection time of 50 ms and a scan range of 400–1,500 m/z. Ions were isolated in a 1.6 m/z window, with an AGC target of 1×10^4 or maximum injection time of 35 ms, fragmented with a normalized collision energy of 30, and the resulting MS2 spectra were obtained in the ion trap. Dynamic exclusion was set to 60 seconds, and ions with a charge state <2, >7 or unknown were excluded. For the overexpression samples, 250 ng of each sample was loaded onto commercial EvoTips according to manufacturer's instructions, and separated over a 2-h gradient using Whisper^{TM} flow operating at 100 nl/min. The Orbitrap Eclipse instrument was run in a MS-OT, ddMS2-IT-HCD top speed method, combined with FAIMSPro operating at 2 CVs (−50 and −70), swapping CV every 2.5 and 1.5 seconds respectively. Full MS spectra were collected at a resolution of 240,000, with an AGC target of 100% or maximum injection time of 50 ms and a scan range of 375–1,500 m/z. Ions were isolated in a 1.4 m/z window, with an AGC target of 300% or maximum injection time of 23 ms, fragmented with

a normalized collision energy of 30, and the resulting MS2 spectra were obtained in the ion trap. MS performance was verified for consistency by running complex cell lysate quality control standards, and chromatography was monitored to check for reproducibility.

Northern blot and rRNA transcript analysis

Unfractionated BM cells and Ter119 enriched BM cells were lysed in Trizol reagent and RNA was isolated by phenol-chloroform extraction. RNA northern hybridizations were performed as previously described (Wang and Pestov, 2016) using oligonucleotide probes shown in Table S6. For quantitative analysis, ratios of different pre-rRNAs in *Ptbp1*^{KO} cells were determined from the northern hybridizations and normalized to the corresponding ratios in *Ptbp1*$^{fl/fl}$ cells (Wang et al., 2014). For Bioanalyzer gel electrophoresis and measurements of total RNA, 5x10^{6} Ter119^{+} cells per sample were sorted and isolated by the RNeasy micro kit (Qiagen).

QUANTIFICATION AND STATISTICAL ANALYSIS

For two-group comparisons, statistical analyses were performed using unpaired, two-tailed Student's t-test if nothing else stated. Details of the specific statistical test used can be found in figure legends. * = P$\leq$ 0.05, ** = P $\leq$0.01, *** = P$\leq$ 0.001, ns = non-significant. For bar-graphs, error bars indicate standard deviation if not stated otherwise. The number of replicates used in experiments are noted in figures, figure legends, or by graphs represented as dot plots, where **n** represents number of biological replicates (i.e. individual mice). For Figures 5 and 7, **n** may represent number of genes or proteins.

RNA-seq differential expression analysis

RNA-seq reads were processed with the bcbio RNA-seq pipeline (https://github.com/bcbio/bcbio-nextgen) and the bcbioRNASeq R package (https://github.com/hbc/bcbioRNASeq) for each of the three populations (HSCs, preMegEs, preCFU-Es) individually. Transcript abundance estimates were obtained using Salmon (v0.12.0 with options quant -l IU –seqBias –gcBias –numBootstraps 30) (Patro et al., 2017) for transcripts defined by ENSEMBL (version 94), summarized to gene level and imported into R using tximport (v1.10.1) (Soneson et al., 2015). Differential gene expression analysis between the *Ptbp1*^{KO} and *Ptbp1*$^{fl/fl}$ genotype was performed using DESeq2 (v1.22.2) with standard parameters (Love et al., 2014). Shrunken log fold changes were used for visualization in the volcano plots and are reported in Table S1. Data has been deposited in the Gene Expression Omnibus (GEO) database (http://www.ncbi.nlm.nih.gov/gds) (Edgar et al., 2002) under the accession number GSE165682. For gene set enrichment analysis (GSEA), results were ranked by Wald statistics, excluding any rows with adjusted p value NA (those that are filtered by DESeq2's automatic independent filtering for having a low mean normalized count). Ensembl genes IDs were mapped to HUGO gene symbols, averaging the Wald statistic when multiple mappings to the same symbol. The MSigDB v7.2 gene sets from the Gene Ontology (C5:GO) and canonical pathways (C2:CP) sub-collections (Liberzon et al., 2011) were used in GSEA-Preranked with classic scoring scheme (Subramanian et al., 2005).

Differential splicing analysis

Raw fastq files were aligned with STAR (Dobin et al., 2013) using default parameters and mapped to the Grc38/mm10 genome. BAM files generated were subsequently used as input for Cuffdiff (Trapnell et al., 2013). To quantify isoforms and splice variant usage differences between *Ptbp1*$^{fl/fl}$ or *Ptbp1*^{KO} cells, IsoformSwitchAnalyzeR (Vitting-Seerup and Sandelin, 2019) v1.9.3 was used with minor modifications to the standard workflow. Genes expressed less than three FPKM and isoforms expressed less than one FPKM and not contributing at least 10% of the total parent gene expression were removed. After this filtering, only genes with at least two transcripts were kept. The statistical analysis of differentially used transcripts was done via DEXSeq (Anders et al., 2012) v1.32.0 by using the isoformSwitchTestDEXSeq() function specifying reduceFurtherToGenesWithConsequencePotential = FALSE. Open reading frames (ORF), Nonsense Mediated Decay (NMD) and AS were identified and analyzed by IsoformSwitchAnalyzeR as described in (Vitting-Seerup and Sandelin, 2019) and (Vitting-Seerup et al., 2014). To describe the transcriptional changes, IsoformSwitchAnalyzeRs analyzeSwitchConsequences() function was used to analyze isoform switches for the following consequences (aka differences): intron retention, nonsense-mediated decay, alternative transcription start and termination sites, changes in the last exon and changes in isoform length and exon number. The genome wide analysis of enrichment of certain consequences or splicing events was done using extractConsequenceEnrichment() and extractSplicingEnrichment() as described in (Vitting-Seerup and Sandelin, 2019).

Label-free quantitative proteomics analysis

The raw files from the PreMegE and preCFUe samples were analyzed using MaxQuant version 1.5.2.8 (Cox and Mann, 2008) and standard settings. Briefly, label-free quantitation (LFQ) was enabled with a requirement of two unique peptides per protein, and iBAQ quantitation was also enabled during the search. Variable modifications were set as Oxidation (M), Acetyl (protein N-term), Gln- > pyro-Glu and Glu- > pyro-Glu. Fixed modifications were set as Carbamidomethyl (C), false discovery rate was set to 1%, and "match between runs" was enabled. The resulting protein groups file was processed with an in-house developed tool (PINT) (Wojtowicz et al., 2016) which imputes missing LFQ values with adjusted iBAQ values. Briefly, the distributions of iBAQ intensities for each sample are adjusted to overlap with the LFQ intensity distributions using median-based adjustment, enabling the direct imputation of missing LFQ values with adjusted iBAQ values for those proteins that did not have LFQ values across all the samples.

By simultaneously filtering for reverse hits and contaminants, this resulted in a final list of 4,847 and 4,990 proteins identified and quantified in preMegE and preCFUe samples respectively. The CDC42 over-expression sample raw files were analyzed using Proteome Discoverer 2.4. Label-free quantitation (LFQ) was enabled in the processing and consensus steps, and spectra were matched against the *Mus musculus* database obtained from Uniprot. Dynamic modifications were set as Oxidation (M), and Acetyl, Met-loss and Met-loss + Acetyl on protein N-termini. Cysteine carbamidomethyl was set as a static modification. All results were filtered to a 1% FDR, and protein quantitation done using the built-in Minora Feature Detector and Precursor Ions Quantifier. The mass spectrometry data have been deposited to the ProteomeXchange Consortium (http://proteomecentral.proteomexchange.org) via the PRIDE (Perez-Riverol et al., 2019) partner repository with the dataset identifier PXD023879.

Analysis of the preMegE transcriptome vs. proteome

Results from RNA- and protein-level differential expression (DE) analysis were mapped based on gene symbols (excluding any ambiguous cases), yielding 4,408 genes. These were ranked by their protein log fold changes ($rank_{protein}$ = 1 for the most down-regulated protein) and by their RNA log fold changes ($rank_{RNA}$ = 1 for the most down-regulated RNA). The rank difference d ($rank_{protein} - rank_{RNA}$) was used to split the data into five classes. After excluding 56 genes due to missing UTR information, the remaining 4,352 genes distribute across the rank classes as follows: Class 1: $d < -2{,}000$ (N = 568), Class 2: $-2{,}000 \leq d < -1{,}000$ (N = 619), Class 3: $-1{,}000 \leq d \leq 1{,}000$ (N = 1941), Class 4: $1{,}000 < d \leq 2{,}000$ (N = 682), Class 5: $2{,}000 < d$ (N = 542).

PTBP1 CLIP data and binding motif analysis

5′-UTR regions for mouse mm9 genome assembly were retrieved from Gencode annotations (release M1), and for each Ensembl gene, the genomic coordinates of the longest 5′-UTR region were determined. Significant crosslink sites identified by (Vuong et al., 2016) were downloaded for PTBP1 KI (GSM2259090) and PTBP2 (GSM2259093), and overlapped with the 5′-UTRs using bedtools intersect (Quinlan and Hall, 2010). Previously identified binding motifs for PTBP1 were extracted from the literature: "HYUUUYU" as identified via RNA-compete (Ray et al., 2013); "UUCUCU" was identified as the most overrepresented motif in PTB-binding clusters in (Xue et al., 2009). Regular expressions of these motifs were screened against the 5′-UTR sequences. Sequences corresponding to the PRTE and TOP motifs were downloaded from (Hsieh et al., 2012) and used to define the position weight matrix (PWM) for PRTE and TOP motifs using seqLogo package in R. The PWMs corresponding to the OP motif (OP_ALL, OP_NARROW and OP_BROAD) were downloaded from (Eliseeva et al., 2013). All PWMs were then searched against the 5′-UTR regions of genes using Homer (findMotifsGenome.pl -size given -seqlogo) (Heinz et al., 2010).

Mapping of K562 eCLIP data to the human rDNA sequence

Fastq files for duplicate eCLIP samples (PTBP1, XRN2, U2AF1) and the associated background control were downloaded from ENCODE (https://www.encodeproject.org) (Experiment identifiers: ENCSR981WKN, ENCSR657TZB and ENCSR862QCH respectively) (Van Nostrand et al., 2020) and mapped to the human 45s pre-ribosomal DNA sequence (RNA45SN5: NR_046,235.3) using STAR (Dobin et al., 2013) with the following options: –limitBAMsortRAM 1038531398 –outFilterMismatchNoverLmax 0.05 –outFilterMatchNmin 40 –outFilterScoreMinOverLread 0 –outFilterMatchNminOverLread 0 –alignIntronMax 1. The number of reads mapped to each region of the 45s pre-ribosomal RNA (5′ ETS: 1–3655, 18s rRNA: 3655–5523, ITS1: 5523–6601, 5.8s rRNA: 6601–6757, ITS2: 6757–7925, 28s: 7925–12994) was determined using bedtools coverage (Quinlan and Hall, 2010). To determine whether binding of any of the analyzed proteins was enriched in specific regions, the 13kb rDNA sequence was divided into 126 tiling regions of 100 bp and the number of reads mapping to each bin was computed. A Fisher's exact test was performed by comparing the percentage of mapping in each bin for the replicate samples and the background control. The odds-ratio for each bin was plotted. Data analysis was performed with R/Bioconductor (https://www.R-project.org) (Gentleman et al., 2004).

Seten

Gene set enrichment analysis of PTBP1 binding of protein-coding transcripts in K562 cells (eCLIP data generated by the ENCODE project (Van Nostrand et al., 2020)) was available through Seten's web interface (Budak et al., 2017).